Article

Developmental Cell

Rho Flares Repair Local Tight Junction Leaks

Graphical Abstract

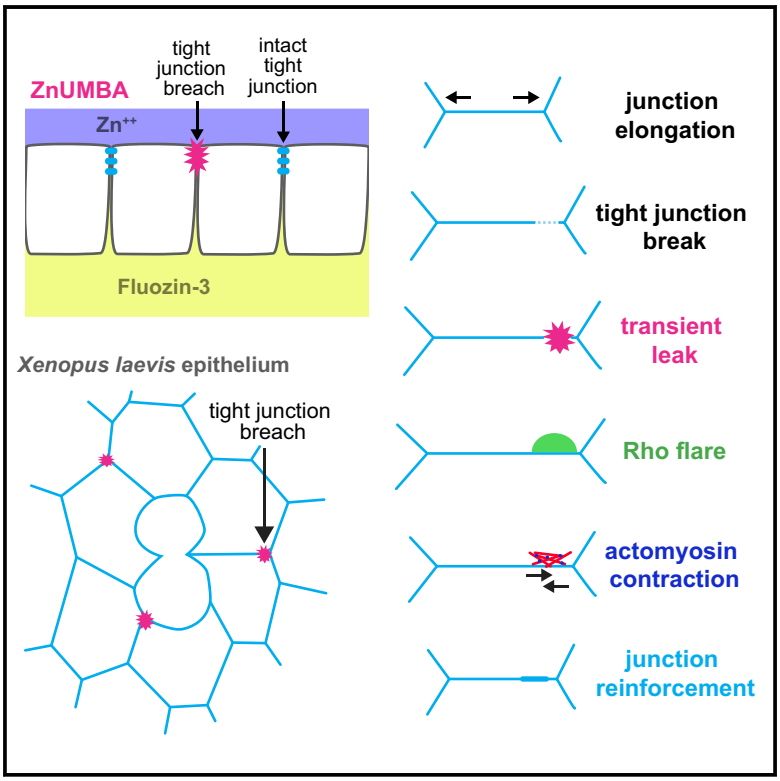

Highlights

- ZnUMBA is a novel zinc-based ultrasensitive microscopic barrier assay
- ZnUMBA detects transient, localized tight junction breaches in developing epithelia
- Rho flares rapidly repair tight junctions to minimize leakiness at breach points
- Actomyosin-mediated junction contraction promotes tight junction reinforcement

Authors

Rachel E. Stephenson, Tomohito Higashi, Ivan S. Erofeev, Torey R. Arnold, Marcin Leda, Andrew B. Goryachev, Ann L. Miller

Correspondence

annlm@umich.edu

In Brief

Epithelial barrier function is critical for normal organ function. Stephenson et al. present a barrier assay capable of detecting transient breaches of the epithelial barrier with high spatial and temporal resolution. Additionally, they find that Rho flares promote actomyosin-mediated junction contraction, which rapidly repairs transient leaks to maintain barrier integrity.

Stephenson et al., 2019, Developmental Cell *48*, 1–15
February 25, 2019
https://doi.org/10.1016/j.devcel.2019.01.016

CellPress

Please cite this article in press as: Stephenson et al., Rho Flares Repair Local Tight Junction Leaks, Developmental Cell (2019), https://doi.org/10.1016/j.devcel.2019.01.016

Developmental Cell
Article

Rho Flares Repair Local Tight Junction Leaks

Rachel E. Stephenson,[1] Tomohito Higashi,[1,3] Ivan S. Erofeev,[2] Torey R. Arnold,[1] Marcin Leda,[2] Andrew B. Goryachev,[2] and Ann L. Miller[1,4,*]

[1]Department of Molecular, Cellular, and Developmental Biology, University of Michigan, Ann Arbor, MI 48109, USA
[2]Centre for Synthetic and Systems Biology, School of Biological Sciences, University of Edinburgh, Edinburgh EH9 3BF, UK
[3]Present address: Department of Basic Pathology, Fukushima Medical University, Fukushima 960-1295, Japan
[4]Lead Contact
*Correspondence: annlm@umich.edu
https://doi.org/10.1016/j.devcel.2019.01.016

SUMMARY

Tight junctions contribute to epithelial barrier function by selectively regulating the quantity and type of molecules that cross the paracellular barrier. Experimental approaches to evaluate the effectiveness of tight junctions are typically global, tissue-scale measures. Here, we introduce Zinc-based Ultrasensitive Microscopic Barrier Assay (ZnUMBA), which we used in *Xenopus laevis* embryos to visualize short-lived, local breaches in epithelial barrier function. These breaches, or leaks, occur as cell boundaries elongate, correspond to visible breaks in the tight junction, and are followed by transient localized Rho activation, or Rho flares. We discovered that Rho flares restore barrier function by driving concentration of tight junction proteins through actin polymerization and ROCK-mediated localized contraction of the cell boundary. We conclude that Rho flares constitute a damage control mechanism that reinstates barrier function when tight junctions become locally compromised because of normally occurring changes in cell shape and tissue tension.

INTRODUCTION

Epithelial tissues generate specialized compartments within multicellular organisms, and disruption in epithelial barrier function is associated with disease (Choi et al., 2017; Ivanov et al., 2010). In vertebrates, tight junction protein complexes regulate the degree to which selected molecules pass between cells in an epithelium. There are at least two well-defined routes for molecules to cross the tight junction barrier: the pore pathway and the leak pathway.

The pore pathway is a high-capacity, highly selective route for small molecules such as water and ions to diffuse across the junction (Shen et al., 2011). The selectivity of the pore pathway is based on the expression of claudin family transmembrane proteins, which oligomerize into strands and form size- and charge-selective extracellular pores that restrict the paracellular passage of molecules (Rosenthal et al., 2017; Van Itallie and Anderson, 2014). Transepithelial electrical resistance (TER) is a commonly used technique to measure changes in the pore pathway at the tissue scale.

The leak pathway is a low-capacity route by which larger molecules, such as proteins and other macromolecules, can cross the tight junction (Shen et al., 2011). There is clear evidence that regulation of the leak pathway is distinct from the pore pathway (Balda et al., 1996; Fanning et al., 2012; Turner et al., 2014; Van Itallie et al., 2009), that is, epithelial tissues can change their permeability to large molecules without affecting the flux of ions and vice versa. One proposed mechanism for the leak pathway is that the sequential breaking and annealing of claudin strands non-specifically allows a small volume of material to cross the junction as though it was passing through a series of gates (Zihni et al., 2016). Claudins that are exogenously expressed in fibroblasts, which do not normally make tight junctions, form strands that demonstrate this type of breaking and annealing dynamics (Sasaki et al., 2003; Van Itallie et al., 2017).

The leak pathway is typically evaluated by adding traceable macromolecules, such as fluorescent dextrans, to the apical surface of an epithelium and measuring their passage to the basal compartment over time, usually on the scale of hours. A drawback of this approach is that it measures global barrier function; it does not reveal where leaks occur, how many there are, or how long they last. Recently developed "sandwich assays" employ avidin- and biotin-labeled molecules applied to either side of the tissue to capture the macromolecules as they cross the tight junction barrier. These studies have revealed that barrier function to macromolecules is not uniform across the cell and tissue level and that the leak pathway opens and closes over time (Dubrovskyi et al., 2013; Ghim et al., 2017; Richter et al., 2016).

Experimental evidence points to F-actin and myosin II as important regulators of the leak pathway (Fanning et al., 2012; Turner et al., 2014; Van Itallie et al., 2015), although the direct mechanism is unknown. Actomyosin is a critical regulator of cell-cell junctions (Arnold et al., 2017), and also facilitates cell shape changes in epithelial tissues, such as cell division, extrusion, and wound healing. Therefore, we hypothesized that actomyosin dynamics associated with cell shape change could trigger the leak pathway.

In a previous study, we examined epithelial barrier function during cytokinesis by directly imaging fluorescein applied to

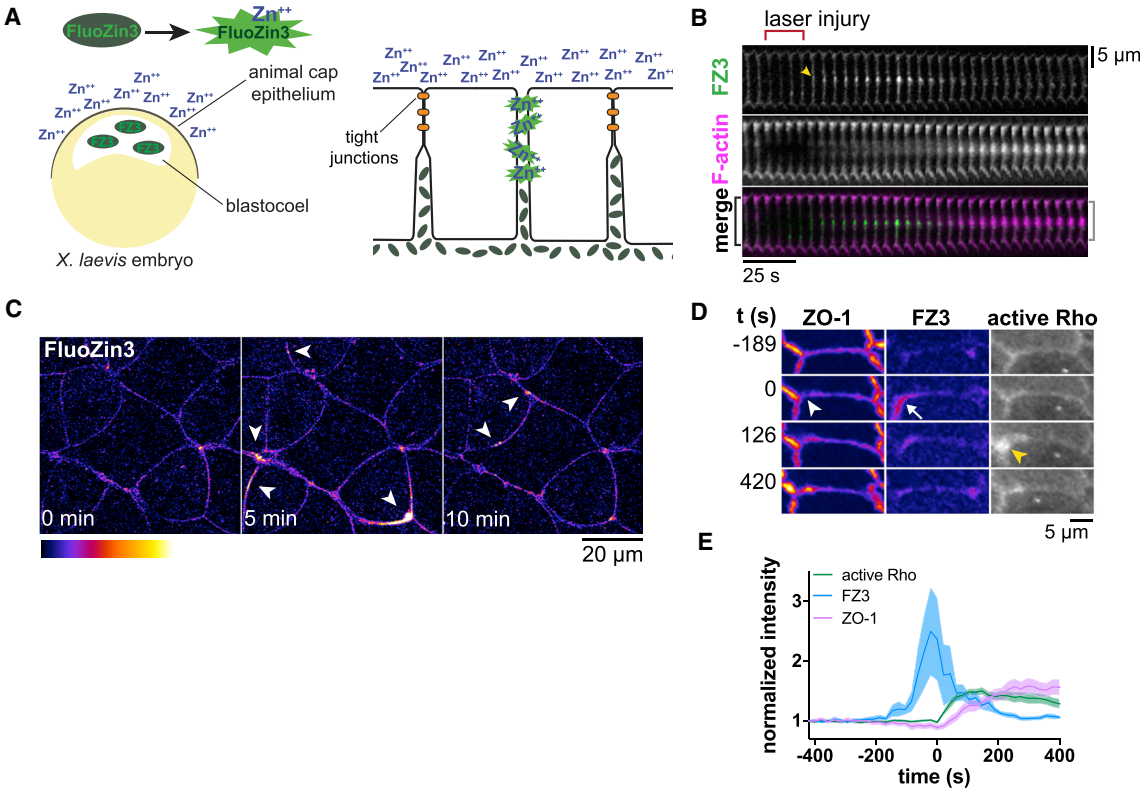

Figure 1. Transient, Localized Leaks in the Tight Junction Barrier Are Followed by Flares of Active Rho and Restoration of Barrier Function

(A) Schematic of Zinc-based Ultrasensitive Microscopic Barrier Assay (ZnUMBA). Exchange of zinc and FluoZin-3 (FZ3) through disrupted tight junctions yields a local increase in FZ3 fluorescence.

(B) Validation of ZnUMBA by laser injury of the junction (red bracket). FZ3 (green) increases in intensity (yellow arrowhead) following laser injury and persists for roughly 75 s. Note that F-actin (Lifeact-RFP, magenta) accumulates at the site of injury, and the junction contracts (black bracket versus gray bracket).

(C) FIRE Lookup Table (LUT) applied to FZ3 in the unperturbed *Xenopus laevis* epithelium. Arrowheads indicate short-lived, localized barrier leaks.

(D) Leaks (FZ3, white arrow) occur at sites of local ZO-1 loss (white arrowhead), and Rho flares (yellow arrowhead) follow at these sites. FZ3 intensity decreases while ZO-1 intensity increases following Rho flares.

(E) Mean normalized intensity for active Rho (mCherry-2xrGBD), FZ3, and ZO-1 (BFP-ZO-1) at the site of the Rho flare over time quantified from (D) and additional videos. Shading represents standard error of the mean (SEM). n = 17, 7, and 5 (flares, embryos, experiments, respectively).

See also Figure S1 and Videos S1, S2, and S3.

the apical surface of a *Xenopus laevis* embryo as a fluorescent tracer (Higashi et al., 2016). We saw no penetrance of the tracer beyond the tight junctions, even at the contractile ring, a site that undergoes a major change in cell shape and represents a potential challenge to junction integrity (Hatte et al., 2018). However, we reasoned that small volumes of the tracer might be difficult to detect against the high background of apical fluorescein. Therefore, we sought to develop a more sensitive barrier assay with minimal background, in which a breach of tight junctions results in strongly increased fluorescence. We achieved this by using the small cell-impermeable dye FluoZin3 (FZ3), which increases in fluorescence more than 50-fold when bound to zinc. By applying FZ3 to the basal medium and adding media containing $ZnCl_2$ to the apical side, localized breaches of the tight junction result in localized increases in FZ3 fluorescence, which can be easily detected with conventional confocal microscopy. We call this assay ZnUMBA (Zinc-based Ultrasensitive Microscopic Barrier Assay) (Figure 1A). Applying ZnUMBA to the intact epithelium of *X. laevis* embryos allowed us to visualize transient leaks in the epithelium and correlate them with local loss of ZO-1 and occludin. Leaks were followed by transient local activation of RhoA, or Rho flares, which reinstated barrier function by locally concentrating tight junction proteins through Rho kinase (ROCK)-mediated contraction of the junction. Rho flares were preceded by junction elongation, indicating that local expansion and contraction of tight junctions is one mechanism that regulates the leak pathway, potentially through local dilution and concentration of tight junction proteins, respectively.

RESULTS

ZnUMBA Detects Transient Leaks That Correspond to Sites of Local Rho Activation

Gastrula-staged *Xenopus laevis* embryos possess a fully polarized epithelium with apical tight junctions facing the external environment, allowing tight junction dynamics to be easily viewed with confocal microscopy while leaving the embryo completely intact. To perform ZnUMBA in *X. laevis*, we microinjected FZ3 into the blastocoel of gastrula-stage embryos and mounted the embryos in media containing $ZnCl_2$

immediately before imaging. First, we tested the sensitivity of the assay by globally and locally perturbing tight junctions. To globally disrupt tight junctions, we incubated embryos in EGTA (Figures S1A and S1B), which disrupts tight and adherens junctions (Pitelka et al., 1983; Rothen-Rutishauser et al., 2002). FZ3 intensity began increasing globally within 2 min of EGTA addition, indicating the high temporal sensitivity of the assay. Next, we disrupted tight junctions locally through laser injury (Figure 1B), which caused FZ3 intensity to rapidly increase at the site of laser injury. Notably, FZ3 intensity returned to baseline levels within minutes, demonstrating the ability of the assay to detect transient leaks. Reinstatement of the barrier was accompanied by an accumulation of F-actin and contraction of the cell boundary (i.e., shortening of the distance between the two vertices), revealing a potential mechanism of barrier reinstatement.

We next applied ZnUMBA to the unperturbed epithelium of gastrula-stage *X. laevis* embryos (Nieuwkoop and Faber stage 10.5–12; Nieuwkoop, 1994). At this stage of *X. laevis* development, epithelial tissue faces challenges to barrier function from cell division (Hatte et al., 2018; Higashi et al., 2016), pulses of contraction induced by calcium transients (Wallingford et al., 2001), and spreading of the epithelial tissue due to gastrulation (Webb and Miller, 2006). We observed sporadic, short-lived local increases in FZ3 signal at cell-cell junctions throughout the animal cap epithelium of the embryo (Figure 1C; Video S1), suggesting that the tight junction barrier is sporadically breached then quickly repaired, consistent with the dynamic strand hypothesis of the leak pathway. As with laser injury, resolution of leaks was frequently associated with junction contraction (Figure S1C). Previous studies have identified that excess paracellular flux of macromolecules is associated with defects in junctional actin accumulation (Fanning et al., 2012; Van Itallie et al., 2015). Therefore, we hypothesized that actin accumulation and/or junction contraction is associated with leak resolution.

The small GTPase RhoA is a master regulator of contractility, stimulating actin polymerization through formins and ROCK-mediated myosin II motor activity (Arnold et al., 2017; Thumkeo et al., 2013). We have previously reported an increase in the number of Rho flares in conditions where actomyosin associated with cell-cell junctions is perturbed genetically (e.g., by anillin knockdown or MgcRacGAP loss of function [Reyes et al., 2014; Breznau et al., 2015]) or where junctions are perturbed mechanically (through cell wounding [Clark et al., 2009]). This, in combination with the accumulation of F-actin and junction contraction associated with the resolution of leaks, led us to hypothesize that Rho flares serve to restore the tight junction barrier. Indeed, when we observed FZ3 together with a probe for active Rho (GFP-rGBD; Rhotekin GTPase Binding Domain [Benink and Bement, 2005]), we found that the increase in FZ3 intensity precedes the increase in active Rho signal and that FZ3 intensity begins to decline as active Rho intensity increases (Figures 1D and 1E; Videos S2 and S3). Moreover, ZO-1 signal appears locally decreased prior to the flare and rises rapidly after the onset of Rho activation (Figures 1D and 1E). Therefore, an attractive possibility is that Rho flares serve as a rapid repair mechanism that restores barrier function when tight junctions become compromised.

Rho Flares Reinforce Tight Junction Proteins Following Local Discontinuities

We next asked whether the local decrease in ZO-1 prior to the flare was indicative of a breakdown of the tight junction protein complex as a whole. We found that both ZO-1 and occludin, but not claudin-6, locally decrease prior to Rho flares (Figures 2A–2D; Video S4). During Rho flares, ZO-1, occludin, and claudin-6 rise rapidly and remain increased, or reinforced, over baseline levels (Figures 2A–2D). In contrast to ZO-1 and occludin, the adherens junction proteins E-cadherin and α-catenin are not visibly decreased prior to Rho flares (Figures 2E and 2F). Prior to Rho flares, there is no sign of separation between the neighboring cell membranes (Figures 3A and 3B), indicating that a defect in cell-cell adhesion is not a primary cause of increased permeability prior to Rho flares. However, both E-cadherin and α-catenin increase in intensity at the site of the flare (Figures 2E and 2F), indicating that the adherens junction is affected by, or perhaps participates in, the Rho flare-associated concentration of tight junction proteins. In contrast to the tight junction and adherens junction proteins we quantified, the intensity of a membrane probe measured at the junction remains stable over the course of the flare (Figure 3A), indicating that the increases in junction protein intensity are not a flare-induced artifact.

Multicellular vertices (places where three or more cells meet) are sites of high tension in epithelial tissues (Higashi and Miller, 2017; Trichas et al., 2012); thus, we hypothesized that multicellular vertices might be particularly prone to disruption and that Rho flares might be more frequent at these sites. Indeed, we found that Rho flares occurred with an average frequency of 0.81 ± 0.07 flares/min at bicellular junctions, versus 1.50 ± 0.21 flares/min at multicellular vertices. Despite this, there is no apparent disruption of the tricellular tight junction- (tTJ-) specific proteins, angulin-1 (LSR) or tricellulin, prior to Rho flares (Figure S2). However, defects in tTJs may be difficult to detect with the limited resolution of standard confocal microscopy. Interestingly, some remodeling of both angulin-1 and tricellulin is apparent during Rho flares, with the tTJs appearing more compact following Rho flares (Figure S2).

We observed that Rho flares are typically asymmetric with respect to the junction, that is, the plasma membrane of one cell protrudes apically over its neighbor (Figures 3A and 3B). Dense, bright active Rho signal is associated with the membrane protrusion, although there is often a lighter haze of active Rho surrounding the dense signal. The protrusion grows as Rho activity increases and retracts as Rho activity declines (Figure 3A). F-actin emanates from the junction in the direction of the membrane protrusion, while myosin II accumulates on the periphery of the flare and flows toward the junction as the flare retracts (Figures 3C–3E, Video S5). Although the mechanical origin of the membrane protrusion remains a subject for further investigation, F-actin and myosin II accumulate on either side of the membrane protrusion (Figure 3E), indicating that tight junction reinforcement is a cooperative process involving adjacent cells. Notably, many of the hallmarks of Rho flares described above, including membrane protrusion, F-actin and active Rho accumulation, and ZO-1 and occludin reinforcement, can be induced by laser injury of the junction (Figure S3). Therefore, it seems that a Rho-mediated contractile response, similar to those observed in single- and multi-cell wound healing, could drive reinforcement

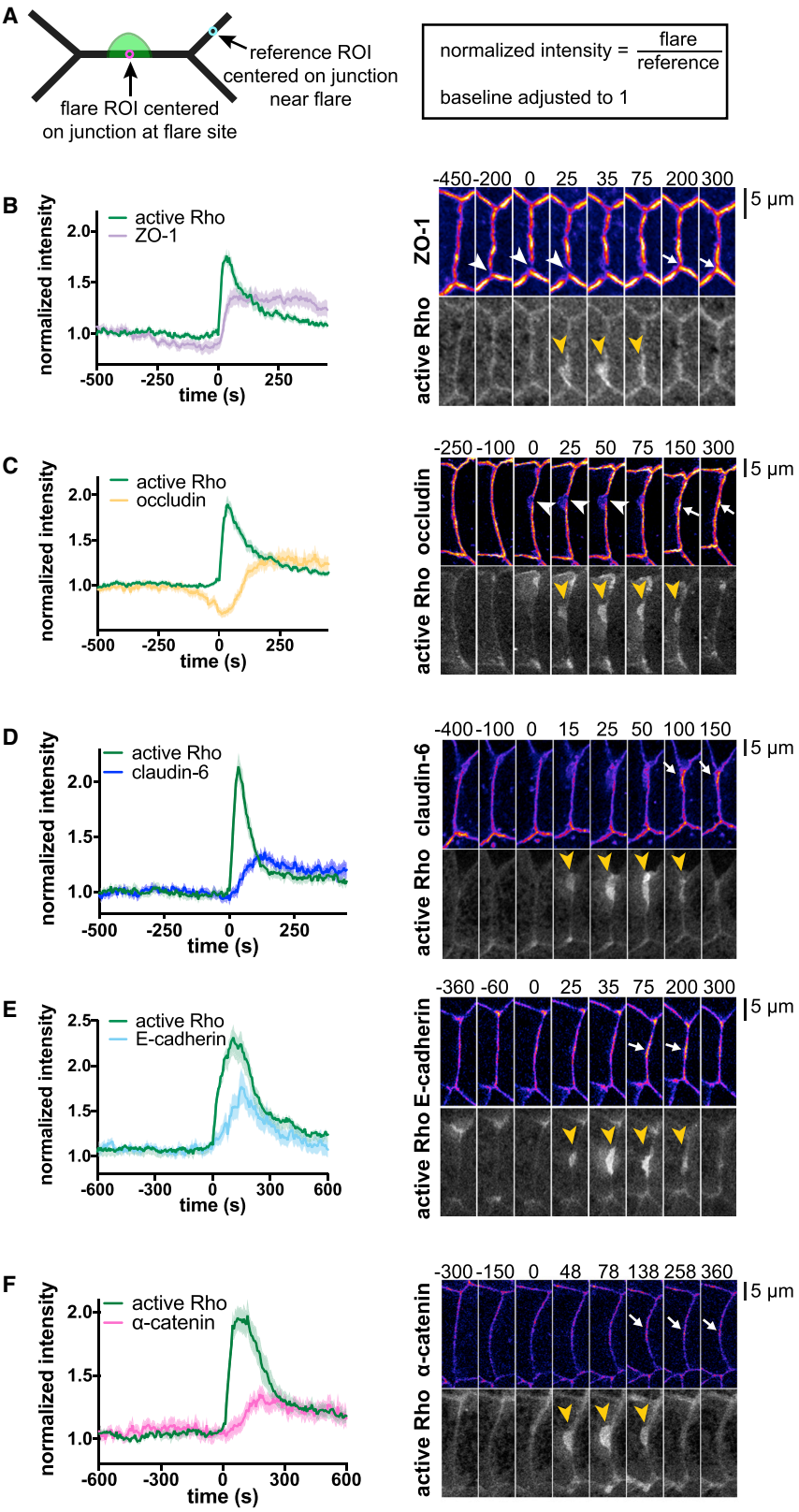

Figure 2. Rho Flares Reinforce Tight Junction Proteins Following Local Discontinuities

(A) Schematic depicting the regions of interest (ROIs) used for calculating normalized intensity at the junction.

(B–F) Left: mean of normalized intensity of a ROI centered on the junction at the site of the flare over time, calculated as depicted in (A). Shading represents SEM. Right: co-imaging of Rho flares with junction proteins. Active Rho is shown in grayscale, all others shown with FIRE LUT. Yellow arrowheads indicate Rho flares, white arrowheads indicate local protein decrease, and white arrows indicate local protein increase. (B) Local decrease in ZO-1 precedes the onset of Rho flares. Following Rho flares, ZO-1 intensity is elevated over baseline. n = 26, 9, and 4 (flares, embryos, experiments, respectively); mRFP-ZO-1, GFP-rGBD. (C) Occludin declines sharply prior to the onset of Rho flares. Following Rho flares, occludin is locally reinforced. n = 28, 7, and 3; mCherry-occludin, GFP-rGBD. (D) Claudin-6 rises during Rho flares and remains reinforced following flares. n = 24, 8, and 3; mCherry-claudin-6, GFP-rGBD. (E) E-cadherin rises during the Rho flares, but returns to baseline levels following flares. n = 22, 7, and 3; E-cadherin-3xmCherry, GFP-rGBD. (F) α-catenin rises during Rho flares and remains reinforced following flares. n = 24, 6, and 3; mCherry-α-catenin, GFP-rGBD.

See also Figure S2 and Video S4.

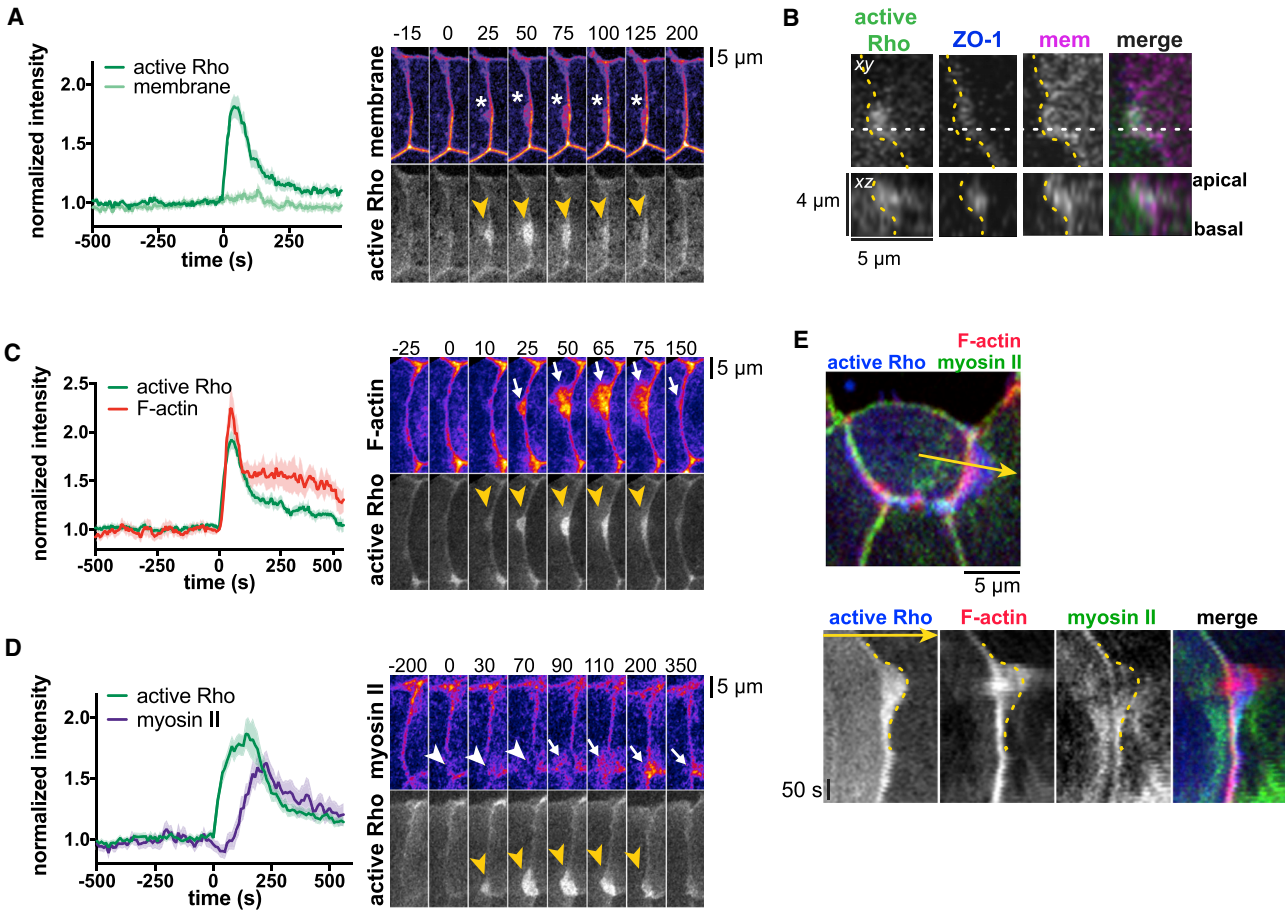

Figure 3. Rho Flares Are Associated with Apical Plasma Membrane Deformations and Accumulation of F-actin and Myosin II

(A, C, D) Left: mean of normalized intensity at the site of the flare over time, as calculated in Figure 2A. Shading represents SEM. Right: co-imaging of Rho flares with membrane, F-actin, or myosin II. Active Rho is shown in grayscale; all others are shown with FIRE LUT. Yellow arrowheads indicate Rho flares, white arrowheads indicate local protein decrease, and white arrows indicate local protein increase. (A) The junctional intensity of the membrane signal stays constant throughout the flare; however, plasma membrane deformations (white asterisks) are associated with Rho flares. n = 25, 9, and 5; mCherry-farnesyl, GFP-rGBD. (B) mCherry-farnesyl (membrane) was expressed mosaically (in cell to the right of the yellow dotted line, which indicates membrane protrusion), while BFP-ZO-1 and GFP-rGBD (active Rho probe) were expressed globally. xz view (made along horizontal white dotted line) shows that the plasma membrane protrudes apically, but not basally. Note that accumulation of active Rho is also apical. (C) F-actin expands in the direction of Rho flares as flares expand and retracts as flares retract. n = 19, 7, and 4; Lifeact-RFP, GFP-rGBD. (D) Junctional myosin II locally decreases at the start of the flare and accumulates on the cortex as Rho flares expand and coalesces toward the junction as flares retract. n = 23, 7, and 3; SF9-mNeon, mCherry-2xrGBD. BFP-ZO-1 (not shown) was used to track the position of the junction.

(E) Top: triple labeling of F-actin (Lifeact-RFP), myosin II (SF9-mNeon), and active Rho (BFP-2xrGBD). Bottom: kymograph generated from the 2-pixel wide yellow line shown in at the top (arrow indicates orientation). Note that F-actin accumulation closely follows the timing and orientation of active Rho, whereas myosin II accumulates at the periphery of the flare and moves toward the junction as the flare retracts. The yellow dotted lines trace the dense accumulation of active Rho, which corresponds to the boundary of the membrane protrusion. Note that both F-actin and myosin II can be seen beyond this boundary, indicating that they also accumulate in the cell neighboring the membrane protrusion.

See also Figure S3 and Video S5.

of tight junction proteins (Benink and Bement, 2005; Clark et al., 2009).

Actin Polymerization Contributes to Tight Junction Reinforcement

Next, we sought to determine how Rho flares contribute to reinforcement of tight junction proteins. Seminal fluorescence recovery after photobleaching (FRAP) studies demonstrated that while claudins are relatively immobile within tight junctions, ZO-1 and occludin are quite dynamic and have different modes of exchange within the junction (Shen et al., 2008). Whereas occludin exchanges by diffusion within the membrane, ZO-1 exchanges with a cytoplasmic pool in a manner dependent on actin polymerization (Shen et al., 2008; Yu et al., 2010). Thus, we hypothesized that actin polymerization and/or junction contraction downstream of Rho flares could contribute to tight junction reinforcement. To distinguish between these possibilities, we first examined ZO-1, an actin-binding protein (Itoh et al., 1997) whose recruitment and stabilization at tight junctions is dependent on actin polymerization (Yu et al., 2010). Co-imaging of active

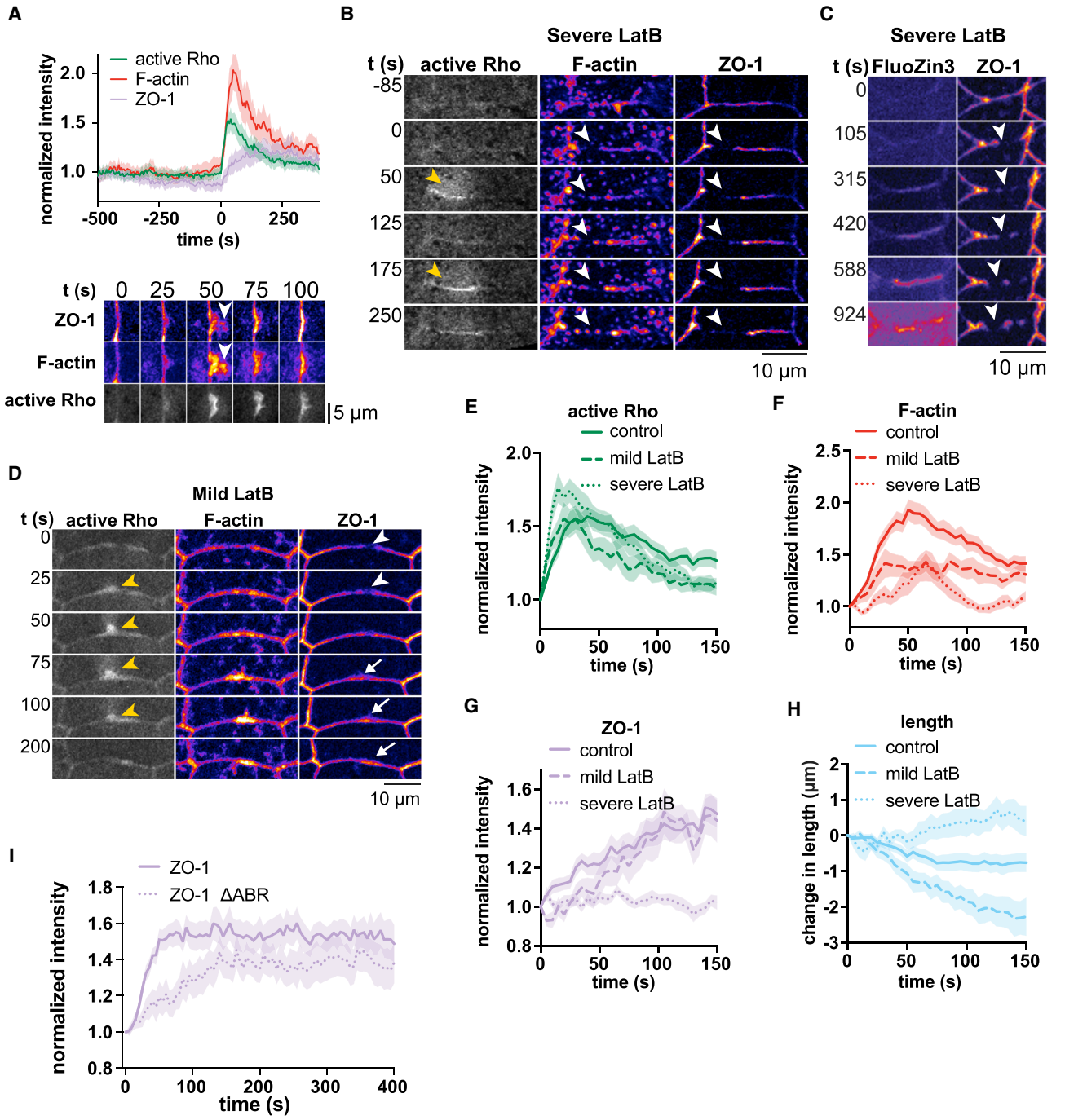

Figure 4. Actin Polymerization and Myosin II-Mediated Contraction Contribute to ZO-1 Reinforcement

(A) Top: mean normalized intensity of active Rho, F-actin, and ZO-1. Shading represents SEM. n = 22, 10, 8 (flares, embryos, and experiments, respectively). Time 0 represents the start of the flare. Bottom: ZO-1 reinforcement closely follows active Rho and F-actin accumulation in space and time. BFP-ZO-1 co-localizes with the actin structures (Lifeact-RFP) emanating from the junction at the site of Rho flares (GFP-rGBD) (white arrowheads).

(B) Incubation with 8–10 μM LatB results in large breaks in junctional F-actin and ZO-1 (white arrowheads). Rho flares (yellow arrowheads) appear at these sites, but no actin polymerization, ZO-1 recruitment, or junction contraction follows, resulting in repeating Rho flares.

(C) The tight junction barrier is not restored in severe LatB conditions. FluoZin3 signal continues to intensify as the discontinuity in ZO-1 (white arrowheads) expands.

(D) Mild (1–5 μM) LatB treatment does not cause disintegration of junctional F-actin, and a subset of junctions rapidly shorten while others rapidly elongate. Rho flares (yellow arrowheads) at these shortening junctions result in ZO-1 reinforcement (white arrows) despite impaired actin polymerization.

(legend continued on next page)

Rho, F-actin, and ZO-1 revealed that ZO-1 accumulation closely follows F-actin accumulation in space and time (Figure 4A), indicating that actin polymerization could feasibly recruit ZO-1 to tight junctions during Rho flares.

To test how actin polymerization affects ZO-1 reinforcement, we treated embryos with Latrunculin B (LatB), which prevents actin polymerization by sequestering G-actin monomers. At 8 μM LatB and higher, we observed a severe effect, which caused large breaks in F-actin and ZO-1 to form, as reported previously (Shen and Turner, 2005) (Figure 4B; Videos S6 and S7). Notably, these breaks were sites of repeated Rho flares, mimicking endogenous Rho flares that appear at sites of decreased ZO-1. Under these circumstances, ZO-1 was not reinforced, and the barrier could not be restored (Figures 4B, 4C, and 4E–4H). Despite the lack of new actin polymerization at Rho flares, existing cortical actin becomes fragmented and forms puncta that are pulled toward the junction where they merge with one another; in rare cases, these junctional accumulations of actin were sufficient to recruit ZO-1 (Video S7). However, junctions elongated during severe LatB treatment (Figure 4H), likely due to the severe disruption of the junctional actin network, so we were not able to distinguish between the contribution of contraction and F-actin polymerization on ZO-1 reinforcement under these conditions.

To avoid completely disrupting junctional F-actin, we reduced the dose of LatB ($\leq$5 μM). Mild LatB treatment results in disruption of tissue integrity, allowing a subset of junctions to rapidly shorten as others elongate to compensate (Video S8). During Rho flares on rapidly shortening junctions, F-actin accumulation is strongly reduced compared to controls (Figures 4D and 4F), and ZO-1 reinforcement is slightly delayed (Figure 4G) but not abolished (Videos S8 and S9). This indicates that junction shortening can compensate for reduced actin accumulation to reinforce ZO-1 (Figures 4E–4H). Furthermore, deletion of the actin-binding region of ZO-1 (Fanning et al., 2002) delayed, but did not abolish, ZO-1 reinforcement (Figure 4I). Taken together, we conclude that actin polymerization contributes to, but is not required for, ZO-1 reinforcement.

ROCK-Mediated Junction Contraction Contributes to Tight Junction Reinforcement

We hypothesized that myosin II-mediated contraction reinforces tight junctions by concentrating proteins within the junction. To test this hypothesis, we generated kymographs of the junction from vertex-to-vertex before, during, and after Rho flares. Kymographs highlighted a variety of Rho flare events, from simple to complex, including isolated Rho flares, repeating flares at a single location, and multiple flares along the same junction (Figure S4A). To simplify the interpretation of length analysis, we initially considered isolated flares. Quantification of these kymographs revealed that the total length of the junction is reduced during Rho flares, and the timing corresponds with the local increase in ZO-1 and occludin (Figures 5A, 5B, S4B, and S4C). Natural variation in junction protein intensity along the junction generates vertical lines in the kymographs that can serve as fiducial position markers. By tracing these lines, we observed that only regions of the junction associated with Rho flares contract, while other regions remain a stable length or elongate (Figures 5A and S4B). This builds on previous work demonstrating that junctions on a given cell can expand and contract independently of one another (Choi et al., 2016) by revealing that subunits *within a junction* can independently expand and contract, and thus force is not equally distributed along a junction. Notably, the analysis of junction length also revealed substantial elongation of the junction prior to flares, suggesting that junction elongation could trigger breaches in the tight junction barrier (Figures 5B and S4C).

To further test whether junction contraction reinforces ZO-1, we inhibited ROCK-mediated myosin II activation with Y-27632, a ROCK inhibitor. Successful cytokinesis and normal junction architecture depend on ROCK; therefore, we used a moderate dose of Y-27632 such that myosin II accumulation at Rho flares was reduced (Figure 5C) without completely disrupting epithelial organization. Y-27632 treatment did not affect F-actin accumulation (Figure 5D). In embryos expressing ZO-1, Y-27632 partially inhibited junction contraction at isolated flares, and ZO-1 reinforcement was reduced (Figures 5E and 5F). In contrast, when embryos expressing occludin were treated with Y-27632, we did not detect a significant decrease in junction contraction or occludin reinforcement at isolated flares (Figures S4D–F). We hypothesized that repeating flares might be a result of a single flare being insufficient to reinforce the barrier, and thus selecting isolated flares may bias the results toward control levels of contraction and reinforcement. When we included more complex flares in the analysis (isolated, repeating, and multiple flares), we observed a significant decline in both junction contraction and occludin reinforcement in Y-27632-treated embryos (Figure S4F). Finally, Y-27632 impaired the efficient restoration of barrier function following Rho flares (Figures 5G and 5H).

Active Rho stimulates actin polymerization through formins and myosin II activation through ROCK. Therefore, we wanted to determine the effect of simultaneously inhibiting formins and ROCK. In order to do this, we employed SMIFH2, a small molecule inhibitor of formins (Rizvi et al., 2009). We validated SMIFH2 for use in *X. laevis* embryos by overexpressing 3xGFP-Dia3, a formin whose ectopic expression induces actin-rich filopodia-like structures in gastrula-stage *X. laevis* embryos (Higashi et al., 2019). SMIFH2, but not DMSO, reduced the size and dynamics of these Dia3-mediated protrusions (Figures S5A and S5B). However, the same concentration of SMIFH2 was not sufficient to consistently diminish actin polymerization at Rho flares (Figures S5C and S5D; data not shown), suggesting either incomplete inhibition of formins or a role for other actin nucleation factors or polymerization enhancers, such as the Arp2/3 complex or Ena/VASP proteins. In concert with SMIFH2, we

(E–H) Quantification of active Rho (GFP-rGBD) (E), F-actin (Lifeact-RFP) (F), ZO-1 (BFP-ZO-1) (G), and junction length (H) in the experiments described above. Controls (untreated embryos): n = 22, 10, and 8; Severe LatB: n = 13, 4, and 2; Mild LatB: n = 12, 5, and 3. Time 0 represents the start of the Rho flare; data are normalized to 1 (E–G) or 0 (H) at time 0. (I) A mutant of ZO-1 that lacks the C-terminal actin-binding region (mRFP-ZO-1 ΔABR) is reinforced more slowly than full length ZO-1 (mRFP-ZO-1).

See also Videos S6, S7, S8, and S9.

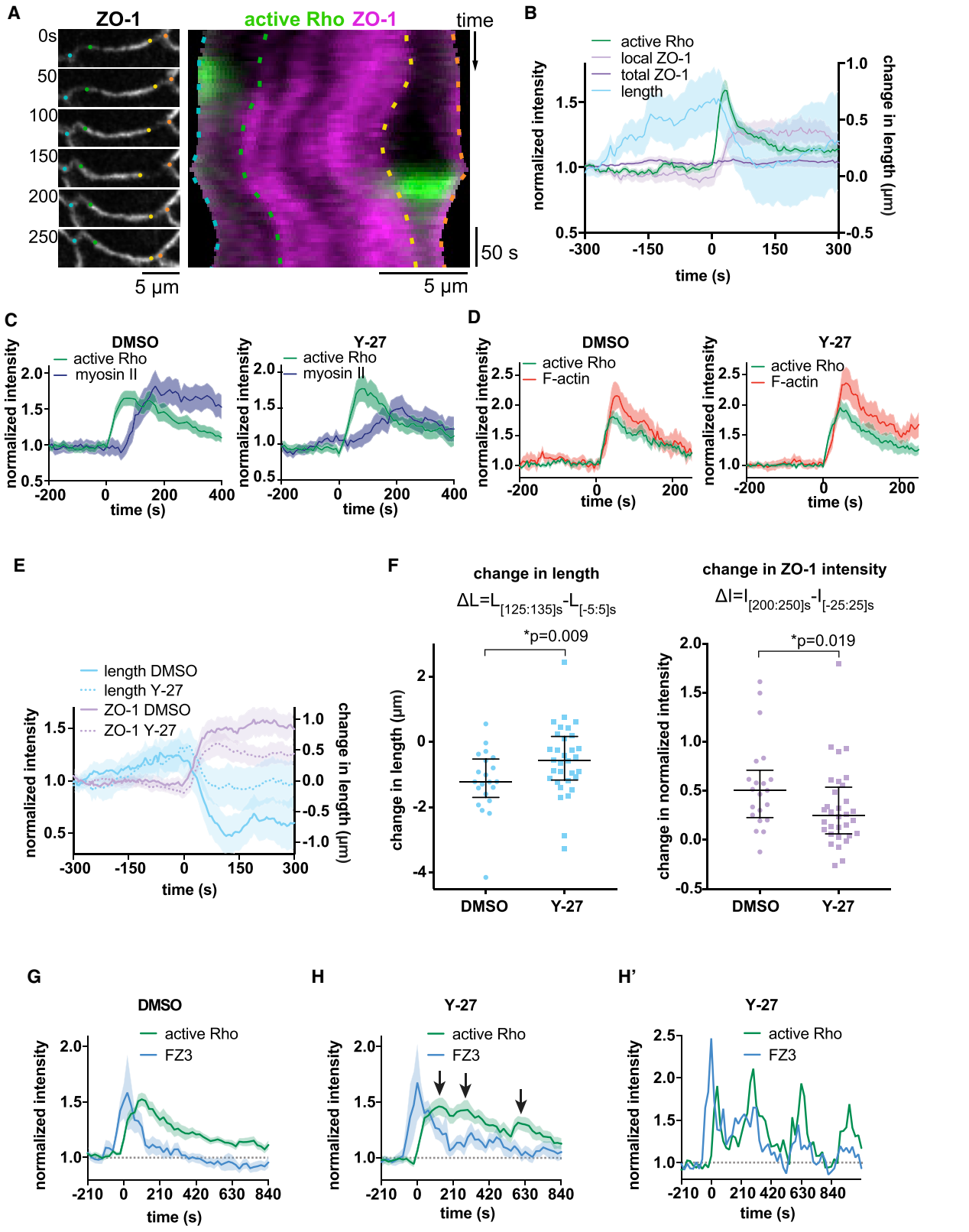

(legend on next page)

employed H-1152, a more potent and specific ROCK inhibitor than Y-27632. Acute treatment with H-1152 dramatically reduced Rho-flare-associated myosin II accumulation at the junction, though not the accumulation of myosin II at the periphery of the flare (Figures S5E–H).

Finally, we tested the effect of SMIFH2 and H-1152 on barrier function and ZO-1 reinforcement (Figure 6). Similar to Y-27632, H-1152 reduced ZO-1 reinforcement relative to control and produced repeating Rho flares (Figures 6A, 6C, and 6D). SMIFH2 modestly decreased ZO-1 reinforcement relative to control (Figures 6A, 6E, and 6F); however, SMIFH2 caused an increase in global FZ3, indicating that formins may be more important for promoting global, sustained barrier function rather than local repair (Figure 6B). Together, SMIFH2 and H-1152 synergistically disrupted global barrier function, although no change in ZO-1 reinforcement relative to H-1152 alone was apparent (Figures 6A, 6B, and 6G). Taken together, these results suggest that formins play an important role in epithelial barrier function, although formin-mediated actin polymerization may be dispensable for Rho flare-mediated tight junction repair. Overall, these findings support a model in which Rho flares promote myosin II-mediated contraction of a subunit within the junction, thereby concentrating junction proteins locally within that region to repair the barrier.

DISCUSSION

In this study, we developed a highly sensitive assay for detecting localized breaches in tight junctions with live confocal microscopy (Figure 1). ZnUMBA employs a commercially available fluorescent dye, FZ3, making it a convenient assay that can be applied to a wide range of model systems. We demonstrated the efficacy of this assay in *X. laevis* embryos by globally disrupting tight junctions with EGTA and locally disrupting them with laser injury (Figures 1B, S1A, and S1B). When we applied ZnUMBA to the unperturbed embryo, we observed transient, localized breaches of the tight junction barrier that correspond to local decreases in the tight junction proteins ZO-1 and occludin (Figures 1D, 1E, 2B, and 2C). Flares of active Rho occur at the leak sites, reinforcing ZO-1 and occludin and restoring tight junction barrier function (Figure 7).

There are two well-defined routes for molecules to cross tight junctions: the pore pathway and the leak pathway. When we perform ZnUMBA in gastrula-stage *X. laevis* embryos, our experimental evidence is not consistent with the conclusion that Zn^{2+} ions pass through the pore pathway. Expression of specific claudin family proteins determines the selectivity of the pore pathway. In the case of gastrula-stage embryos, the most highly expressed claudins are claudin-6, claudin-7, and, claudin-4 (Session et al., 2016), none of which are known cation pores (Günzel and Yu, 2013). Additionally, overexpression of claudin-2, a cation pore-forming claudin, did not increase FZ3 fluorescence in *X. laevis* embryos (data not shown), suggesting that Zn^{2+} does not pass through claudin pores. When we perform ZnUMBA, embryos are exposed to Zn^{2+} acutely for less than one h, but it should be noted that over long time courses (6–48 h), different studies have found that Zn^{2+} can both enhance and diminish epithelial barrier function (Shao et al., 2017; Wang et al., 2013; Xiao et al., 2018). Thus, when applying the ZnUMBA technique to other model systems, we suggest exposing epithelial cells to Zn^{2+} for the shortest time and lowest dose possible.

Imaging the Leak Pathway: ZnUMBA Allows for Live Imaging of Local Barrier Breaches

Of the two routes for molecules to cross tight junctions, the molecular mechanism of the leak pathway remains elusive. It has been hypothesized that claudin strands break and anneal, forming a series of gates that open and close to allow macromolecules past the tight junction while maintaining a seal of the paracellular space (Zihni et al., 2016). The dynamic breaking and annealing of claudin strands has been visualized in fibroblasts that do not normally form tight junctions (Sasaki et al., 2003; Van Itallie et al., 2017), and perturbing coupling of claudin-2 strands to F-actin through ZO-1 altered strand stability (Van Itallie et al., 2017). However, the dynamic strand hypothesis has not been verified in epithelial tissue because resolving individual claudin strands within the tight junction with light microscopy is difficult due to their tight packing, and, until now, a sensitive assay for visualizing lapses in barrier function did not exist.

Many have speculated that tissue integrity and epithelial barrier function are challenged by naturally occurring changes in tensile force, whether due to cytokinesis, development, or

Figure 5. Junction Contraction Concentrates ZO-1 within the Junction and Is Required for Efficient Reinforcement of the Barrier

(A) Left: montage of the junction that is shown as a kymograph on the right. Colored dots on the montage correspond to the relative position of dashed lines on the kymograph, which trace fiducial marks. Right: kymograph of active Rho (GFP-rGBD, green) and mRFP-ZO-1 (magenta) shows ZO-1 signal increasing as the junction contracts locally.

(B) Quantification of junction length and protein intensity from multiple kymographs. Shading represents SEM. Time 0 corresponds to the start of the Rho flare. Decrease in junction length after the Rho flare aligns with increased local ZO-1 intensity, while total ZO-1 intensity does not increase. n = 19, 6, and 3 (flares, embryos, experiments, respectively).

(C) Quantification of junctional myosin II accumulation at flares in embryos treated with vehicle (DMSO) or ROCK inhibitor (Y-27632 [Y-27]). DMSO: n = 21, 10, and 2; Y-27: n = 18, 7, and 2. SF9-mNeon, mCherry-2xrGBD.

(D) Quantification of junctional F-actin accumulation at flares in embryos treated with DMSO or Y-27632. DMSO: n = 8, 3, and 2; Y-27: n = 20, 7, and 2. Lifeact-RFP, GFP-rGBD.

(E) Junction length versus mRFP-ZO-1 reinforcement in embryos injected with DMSO or Y-27632. Y-27632 partially inhibits junction contraction, and ZO-1 reinforcement is reduced. Vehicle: n = 21, 9, and 3; ROCK inhibitor: n = 32, 7, and 4.

(F) Change in length and intensity were calculated from (E). Significance calculated using Mann-Whitney U test. Bars indicate median and interquartile range.

(G and H) Restoration of the barrier is less efficient in embryos treated with Y-27632 (H) versus DMSO (G). In Y-27632-treated embryos, Rho flares (mCherry-2xrGBD) frequently repeat at the same site—arrows in (H) indicate multiple peaks of active Rho—and FZ3 takes longer to return to baseline (dotted horizontal line). n = 19, 6, and 3 (G) and 18, 4, and 3 (H).

(H′) shows an individual example of a junction with repeated flares.

See also Figure S4.

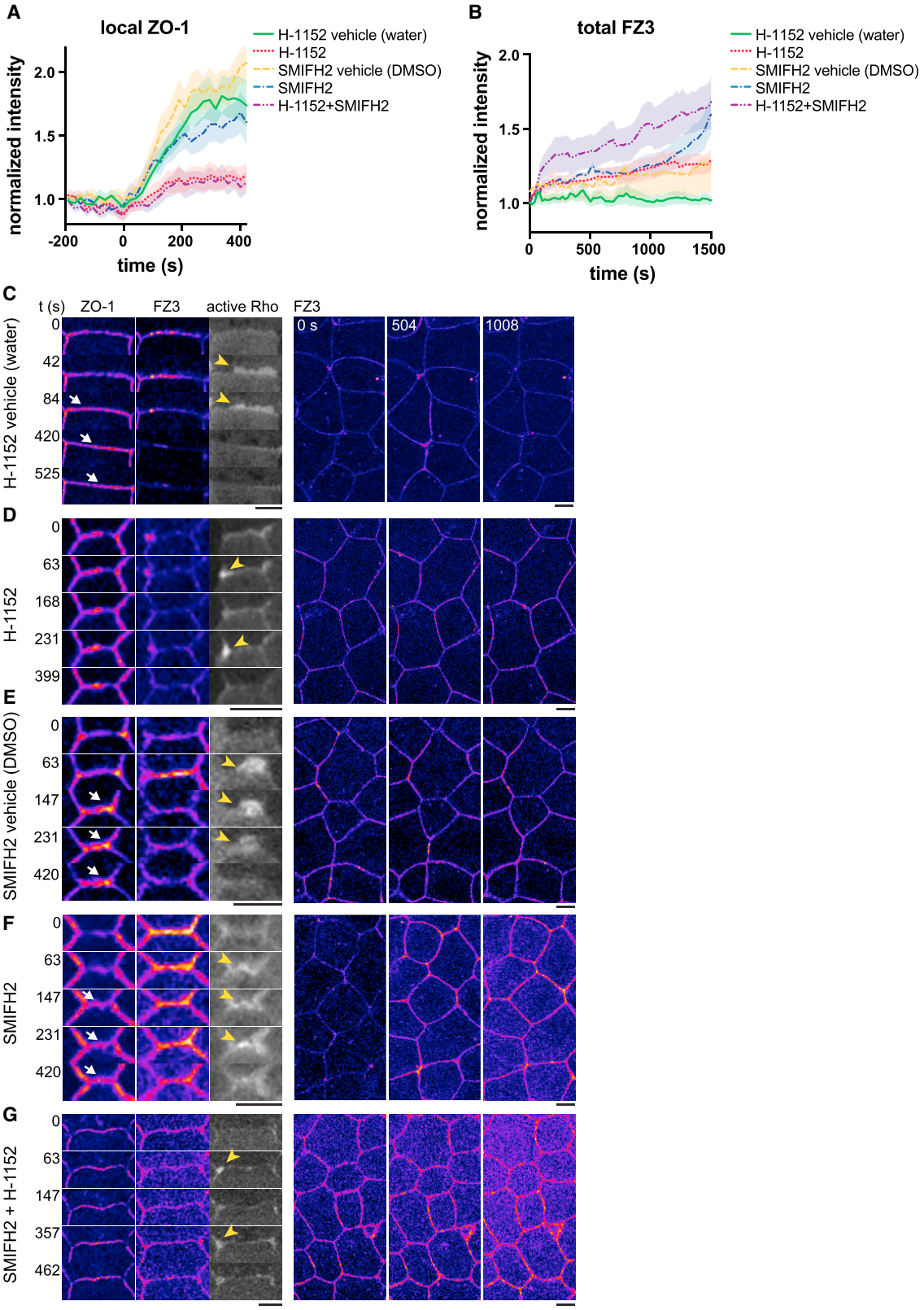

Figure 6. Formins and ROCK Have Distinct Roles in Promoting Barrier Function

Embryos were acutely treated with the ROCK inhibitor H-1152, the formin inhibitor SMIFH2, their respective vehicles (water or DMSO), or both H-1152 and SMIFH2 prior to live imaging.

(legend continued on next page)

normal organ function (Arnold et al., 2017; Charras and Yap, 2018;Hatte et al., 2018). However, direct evidence that barrier function suffers because of these activities has been lacking. Using ZnUMBA to visualize leaks in real time, we were able to reveal new insights about the impact that cell-shape change and local remodeling of the cytoskeleton have on causing and resolving leaks. The localized, short-lived breaches in tight junctions we detected with ZnUMBA were preceded by elongation of the junction and were resolved when flares of active Rho caused localized accumulation of F-actin and myosin II, along with contraction of the junction (Figure 7). Our study revealed that barrier breaches were associated with localized decreases in ZO-1 and occludin, proteins that, along with F-actin and myosin II, are associated with restricting paracellular flux of macromolecules (Balda et al., 1996; Fanning et al., 2012; Turner et al., 2014; Van Itallie et al., 2009). Notably, claudin-6 signal remains unaffected prior to Rho flares, leaving us to speculate whether the barrier to ions is compromised prior to Rho flares. If not, this could explain the seemingly paradoxical findings that paracellular flux of macromolecules can be affected without affecting ion flux (Choi et al., 2016; Fanning et al., 2012; Turner et al., 2014; Van Itallie et al., 2015). Indeed, changes in the intermolecular associations between claudins, ZO-1, occludin, and the actin cytoskeleton are linked to leak pathway regulation and increased strand dynamics (Van Itallie et al., 2017; Yu et al., 2010); therefore, localized decline in ZO-1 and occludin may indicate a molecular basis for the increase in permeability to FZ3. We suggest that our study uncovers one mechanism through which the leak pathway is locally regulated in epithelial cells.

Perturbations That Increase the Tight Junction Leak Pathway Globally or Locally

Global perturbations that increase the leak pathway have been reported. In a study using MDCK II cells, double knockdown (dKD) of ZO-1 and ZO-2 increases flux of larger molecules while preserving TER (Choi et al., 2016; Fanning et al., 2012). This is associated with decreased occludin, increased junctional actin and myosin II accumulation through Shroom3-mediated ROCK recruitment, expansion of the apical domain, and more linear junctions. In a second study, knockout (KO) of TOCA-1, a ZO-1-binding protein and regulator of actin polymerization, shared many phenotypes with ZO-1/2 dKD, including increased macromolecular flux, while preserving TER, as well as decreased membrane contact dynamics (Van Itallie et al., 2015). Although the precise role of the membrane protrusions we observe at Rho flares is unclear, it is notable that actin-dependent membrane dynamics at cell-cell contacts are important for limiting paracellular flux in MDCK II cells (Van Itallie et al., 2015). Thus, we propose that one function of the membrane protrusions at Rho flares may be to temporarily seal the paracellular space while the tight junction is reinforced via the Rho flare. A third study demonstrated that tumor necrosis factor alpha (TNF-α)-induced barrier dysfunction in the intestinal epithelium results in myosin light chain kinase (MLCK)-dependent myosin II activation, contraction of the apical actomyosin array, and occludin endocytosis, which predominantly affects the leak but not the pore pathway (Turner et al., 2014). That global, sustained changes in ZO proteins and occludin result in sustained and presumably global increases in macromolecular flux indicates that local transient loss of these proteins could be involved in local transient increases in macromolecular flux. Indeed, our study suggests that junction elongation, which may be caused by cell-shape changes such as cell division, extrusion, wound healing, or developmental morphogenesis, triggers local breaches in tight junction barrier.

Currently, our understanding of how perturbations such as ZO dKD, TOCA-1 KO, or TNF-α treatment affect the leak pathway is limited. For example, macromolecular flux could increase because of an increase in the number of leak sites, defective resolution of leaks, or a combination of the two. Thus, assays such as ZnUMBA, which allow us to visualize and quantify leaks in space and time, will aid in our understanding of the leak pathway regulation. Interestingly, both ZO-1/2 dKD and TNF-α treatment increase contractility, which could cause strand reorganization or breakage, as seen in freeze-fracture studies (Hull and Staehelin, 1976; Pitelka and Taggart, 1983). Alternatively, the high global contractility in these tissues may make Rho flare-mediated leak resolution more difficult, that is, Rho flares may not generate sufficient contractility to reinforce ZO-1 and occludin when global contractility is already elevated. Similarly, perturbations that reduce tension globally could also cause insufficient Rho flare-mediated contractility to reinforce tight junctions. Understanding the interplay between tissue-scale tension and locally generated tension will be key to understanding local changes in barrier function.

The Case for Measuring Spatiotemporal Dynamics of Junctional Rho Activation

Steady-state Rho activation is important for proper junction structure; however, too much or too little Rho activation can have detrimental effects on barrier function (Quiros and Nusrat, 2014) and is associated with inflammatory diseases (Capaldo and Nusrat, 2009). Our results show that dynamic local Rho

(A) Mean normalized intensity of ZO-1 during Rho flares (active Rho lines omitted for clarity). Flares begin at t = 0 s. H-1152 vehicle (water): n = 24, 9, and 4 (flares, embryos, experiments, respectively); H-1152: n = 22, 8, and 4; SMIFH2 vehicle (DMSO): n = 23, 7, and 3; SMIFH2: n = 25, 7, and 3; SMIFH2+H-1152: n = 26, 9, and 3. Shading represents SEM.

(B) Mean normalized intensity of whole-field FZ3 with the indicated treatments. FZ3 intensity was normalized to the first frame of each movie. t = 0 corresponds to the start of image acquisition. H-1152 vehicle: n = 11 and 4 (embryos and experiments, respectively); H-1152: n = 9 and 3; SMIFH2 vehicle: n = 9 and 3; SMIFH2: n = 6 and 3; SMIFH2+H-1152: n = 9 and 3.

(C–G) Left: co-imaging of active Rho (grayscale), ZO-1, and FZ3 (both shown with FIRE LUT) with the indicated treatments. Yellow arrowheads indicate flares, and white arrows indicate local ZO-1 increase. Right: whole-field FZ3 signal over time. (C) Embryos treated with H-1152 vehicle (water) exhibit normal junction reinforcement and restoration of barrier function following Rho flares. (D) Embryos treated with H-1152 exhibit repeating Rho flares at the same location and reduced ZO-1 reinforcement. (E) Embryos treated with SMIFH2 vehicle (DMSO) exhibit normal junction reinforcement and restoration of barrier function following Rho flares. (F) Embryos treated with SMIFH2 exhibit local ZO-1 reinforcement following Rho flares, but continuous global increase in FZ3 signal. (G) Embryos treated with both SMIFH2 and H-1152 exhibit both repeating Rho flares, reduced ZO-1 reinforcement, and globally increasing FZ3 signal. Scale bars represent 10 μm.
See also Figure S5.

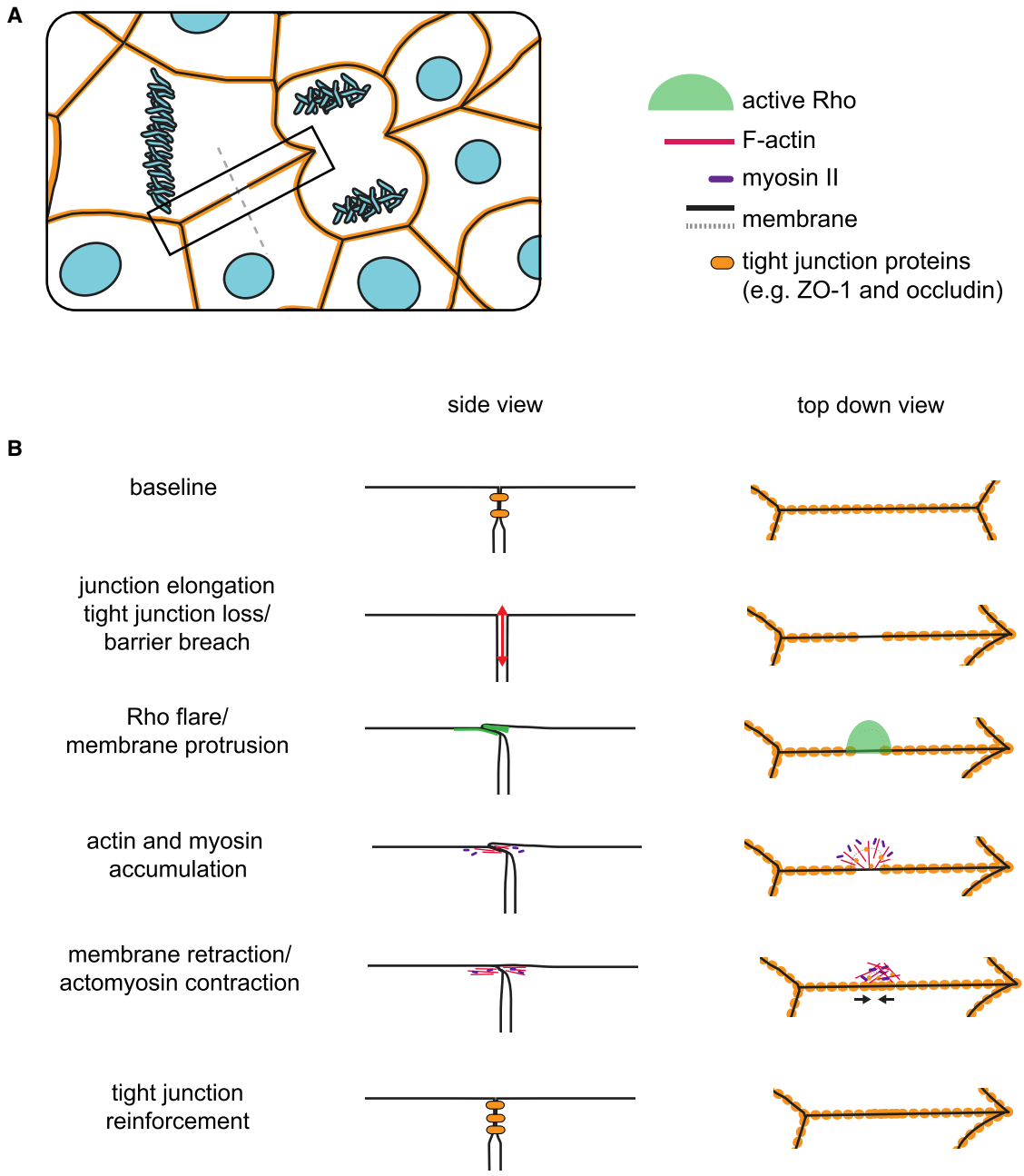

Figure 7. Model of How Rho Flares Reinforce Tight Junction Proteins Following Junction Breaches

A cell- and tissue-scale model of how Rho flares reinforce the epithelial barrier.

(A) Epithelial cells undergo cell shape changes (e.g., as a result of cytokinesis), and epithelial cell-cell junctions must adapt to these cell shape changes.

(B) Local loss of tight junction proteins following junction elongation results in a leaky barrier. Flares of active Rho appear at the site of barrier loss, and the tight junction is reinforced through actomyosin-mediated contraction of the junction. Left: cross-section of the junction corresponding to the gray dashed line in (A). Right: *en face* model of the region outlined in the black box in (A).

flares are important for maintaining epithelial barrier function, and thus measuring total pools of active Rho with biochemical assays, or even imaging active Rho with a snapshot in time is insufficient to capture the whole picture of how Rho activity affects epithelial junctions.

We noted that treating embryos with the formin inhibitor SMIFH2 did not consistently diminish actin polymerization at Rho flares, suggesting the possibility that Arp2/3 and/or other actin nucleation factors or polymerization enhancers might also be involved in promoting the membrane protrusions associated with Rho flares. Indeed, in the context of cell migration, several Rho GTPases collaborate to promote membrane protrusion at the leading edge of migrating cells (Machacek et al., 2009). RhoA promotes the initial protrusion event, and

Rac1 and Cdc42 are activated subsequent to Rho in order to promote stabilization of the protrusion (Machacek et al., 2009). Future studies should investigate the possibility of spatiotemporal coordination among Rho GTPases during the course of Rho flares.

In mature cultured epithelia, levels of active Rho have been reported to be stable over short timescales (Priya et al., 2015). However, our data indicate that active Rho dynamics are important for maintaining barrier function in a developing vertebrate epithelium, in which cells are undergoing shape changes from cell divisions as well as morphogenesis of the embryo. Epithelia in adult organisms also undergo high rates of cell division and cell extrusion, as epithelial tissues experience relatively high rates of cell turnover (Hooper, 1956; Macara et al., 2014). Indeed, other groups have reported short-lived, localized accumulation of F-actin and/or myosin II at junctions in *Drosophila* and cultured mammalian epithelial and endothelial cells during junction remodeling, indicating that Rho flare-like events may be a conserved process (Abu Taha et al., 2014; Pope and Harris, 2008; Razzell et al., 2014; Tokuda et al., 2016). Thus, we propose that the Rho flare mechanism described here may be broadly important for maintaining normal barrier function in developing and adult tissues. As small molecule inhibitors that target Rho and ROCK have been developed to treat diseases that result from barrier dysfunction (Deng et al., 2011; Feng et al., 2016), it will be important to consider that Rho-mediated local junction reinforcement contributes to barrier function.

Concluding Remarks

Collectively, these findings advance our understanding of how epithelia maintain overall barrier function while remaining plastic enough to allow for cell-shape changes. Many excellent studies have explored how cell-cell junctions are remodeled in response to tension (Acharya et al., 2018; Choi et al., 2016; Leerberg et al., 2014; Oda et al., 2014). However, these studies tend to use global, long-term perturbations to increase or reduce tension. Here, we examined junction remodeling in response to endogenous cell- and tissue-scale forces that naturally occur within the developing frog embryo. We found that junction elongation can locally compromise the barrier properties of the epithelium; however, Rho flares restore the barrier on the order of minutes, so that small leaks do not pose a serious threat to epithelial homeostasis.

STAR★METHODS

Detailed methods are provided in the online version of this paper and include the following:

- KEY RESOURCES TABLE
- CONTACT FOR REAGENT AND RESOURCE SHARING
- EXPERIMENTAL MODEL AND SUBJECT DETAILS
- METHOD DETAILS
  - Generation of New DNA Constructs
  - mRNA Preparation and Microinjection
  - Live Imaging
  - Zinc-Based Ultrasensitive Microscopic Barrier Assay
  - Drug Treatments
  - Junction Injury
- QUANTIFICATION AND STATISTICAL ANALYSIS
  - Figure Preparation
  - Manual Quantification of Flares
  - Kymograph Construction and Analysis
  - Calculation of Flare Frequency
  - Statistics
- DATA AND SOFTWARE AVAILABILITY

SUPPLEMENTAL INFORMATION

Supplemental Information includes five figures and nine videos and can be found with this article online at https://doi.org/10.1016/j.devcel.2019.01.016.

ACKNOWLEDGMENTS

We would like to thank members of the Miller lab for discussion and comments on the manuscript, W.M. Bement for the mCherry-2xrGBD and BFP-2xrGBD constructs. This work was funded by NIH grant R01GM112794 to A.L.M. and BBSRC grants BB/P006507 and BB/P01190X to A.B.G. R.E.S. and T.R.A. were supported by NSF Graduate Research Fellowships (DGE #1256260). T.H. was supported by a postdoctoral fellowship from the Japan Society for the Promotion of Science.

AUTHOR CONTRIBUTIONS

Conceptualization, R.E.S., T.H., and A.L.M.; Methodology, R.E.S., T.H., I.S.E., T.R.A., and M.L.; Software, I.S.E. and M.L.; Formal Analysis, R.E.S. and I.S.E.; Investigation, R.E.S. and T.H.; Resources, R.E.S., T.H., and T.R.A.; Writing – Original Draft, R.E.S. and A.L.M.; Writing – Reviewing & Editing, all authors; Visualization, R.E.S. and I.S.E.; Supervision, A.L.M. and A.B.G.; Funding Acquisition, A.L.M. and A.B.G.

DECLARATION OF INTERESTS

The authors declare no competing interests.

Received: May 31, 2018
Revised: November 12, 2018
Accepted: January 17, 2019
Published: February 14, 2019

REFERENCES

Abu Taha, A., Taha, M., Seebach, J., and Schnittler, H.J. (2014). ARP2/3-mediated junction-associated lamellipodia control VE-cadherin-based cell junction dynamics and maintain monolayer integrity. Mol. Biol. Cell *25*, 245–256.

Acharya, B.R., Nestor-Bergmann, A., Liang, X., Gupta, S., Duszyc, K., Gauquelin, E., Gomez, G.A., Budnar, S., Marcq, P., Jensen, O.E., et al. (2018). A mechanosensitive RhoA pathway that protects epithelia against acute tensile stress. Dev. Cell *47*, 439–452.e6.

Arnold, T.R., Shawky, J.H., Stephenson, R.E., Dinshaw, K.M., Higashi, T., Huq, F., Davidson, L.A., and Miller, A.L. (2019). Anillin regulates epithelial cell mechanics by structuring the medial-apical actomyosin network. eLife *8*, e39065.

Arnold, T.R., Stephenson, R.E., and Miller, A.L. (2017). Rho GTPases and actomyosin: partners in regulating epithelial cell-cell junction structure and function. Exp. Cell Res. *358*, 20–30.

Balda, M.S., Whitney, J.A., Flores, C., González, S., Cereijido, M., and Matter, K. (1996). Functional dissociation of paracellular permeability and transepithelial electrical resistance and disruption of the apical-basolateral intramembrane diffusion barrier by expression of a mutant tight junction membrane protein. J. Cell Biol. *134*, 1031–1049.

Benink, H.A., and Bement, W.M. (2005). Concentric zones of active RhoA and Cdc42 around single cell wounds. J. Cell Biol. *168*, 429–439.

Breznau, E.B., Semack, A., Higashi, T., and Miller, A.L. (2015). MgcRacGAP restricts active RhoA at the cytokinetic furrow and both RhoA and Rac1 at cell-cell junctions in epithelial cells. Mol. Biol. Cell *26*, 2439–2455.

Capaldo, C.T., and Nusrat, A. (2009). Cytokine regulation of tight junctions. Biochim. Biophys. Acta *1788*, 864–871.

Charras, G., and Yap, A.S. (2018). Tensile forces and mechanotransduction at cell-cell junctions. Curr. Biol. *28*, R445–R457.

Choi, W., Acharya, B.R., Peyret, G., Fardin, M.A., Mège, R.M., Ladoux, B., Yap, A.S., Fanning, A.S., and Peifer, M. (2016). Remodeling the zonula adherens in response to tension and the role of afadin in this response. J. Cell Biol. *213*, 243–260.

Choi, W., Yeruva, S., and Turner, J.R. (2017). Contributions of intestinal epithelial barriers to health and disease. Exp. Cell Res. *358*, 71–77.

Clark, A.G., Miller, A.L., Vaughan, E., Yu, H.Y., Penkert, R., and Bement, W.M. (2009). Integration of single and multicellular wound responses. Curr. Biol. *19*, 1389–1395.

Davenport, N.R., Sonnemann, K.J., Eliceiri, K.W., and Bement, W.M. (2016). Membrane dynamics during cellular wound repair. Mol. Biol. Cell *27*, 2272–2285.

Deng, J., Feng, E., Ma, S., Zhang, Y., Liu, X., Li, H., Huang, H., Zhu, J., Zhu, W., Shen, X., et al. (2011). Design and synthesis of small molecule RhoA inhibitors: a new promising therapy for cardiovascular diseases? J. Med. Chem. *54*, 4508–4522.

Dubrovskyi, O., Birukova, A.A., and Birukov, K.G. (2013). Measurement of local permeability at subcellular level in cell models of agonist- and ventilator-induced lung injury. Lab. Invest. *93*, 254–263.

Fanning, A.S., Ma, T.Y., and Anderson, J.M. (2002). Isolation and functional characterization of the actin binding region in the tight junction protein ZO-1. FASEB J. *16*, 1835–1837.

Fanning, A.S., Van Itallie, C.M., and Anderson, J.M. (2012). Zonula occludens-1 and -2 regulate apical cell structure and the zonula adherens cytoskeleton in polarized epithelia. Mol. Biol. Cell *23*, 577–590.

Feng, Y., LoGrasso, P.V., Defert, O., and Li, R. (2016). Rho kinase (ROCK) inhibitors and their therapeutic potential. J. Med. Chem. *59*, 2269–2300.

Genovesio, A. (2009). Active Vector Graph for Regularized Tesselation. Proceedings of the 16th IEEE International Conference on Image Processing (ICIP), pp. 2429–2432.

Ghim, M., Alpresa, P., Yang, S.W., Braakman, S.T., Gray, S.G., Sherwin, S.J., van Reeuwijk, M., and Weinberg, P.D. (2017). Visualization of three pathways for macromolecule transport across cultured endothelium and their modification by flow. Am. J. Physiol. Heart Circ. Physiol. *313*, H959–H973.

Günzel, D., and Yu, A.S.L. (2013). Claudins and the modulation of tight junction permeability. Physiol. Rev. *93*, 525–569.

Hatte, G., Prigent, C., and Tassan, J.P. (2018). Tight junctions negatively regulate mechanical forces applied to adherens junctions in vertebrate epithelial tissue. J. Cell. Sci. *131*, jcs208736.

Higashi, T., and Miller, A.L. (2017). Tricellular junctions: how to build junctions at the TRICkiest points of epithelial cells. Mol. Biol. Cell *28*, 2023–2034.

Higashi, T., Arnold, T.R., Stephenson, R.E., Dinshaw, K.M., and Miller, A.L. (2016). Maintenance of the epithelial barrier and remodeling of cell-cell junctions during cytokinesis. Curr. Biol. *26*, 1829–1842.

Higashi, T., Stephenson, R.E., and Miller, A.L. (2019). Comprehensive analysis of formin localization in Xenopus epithelial cells. Mol. Biol. Cell *30*, 82–95.

Hooper, C.E. (1956). Cell turnover in epithelial populations. J. Histochem. Cytochem. *4*, 531–540.

Hull, B.E., and Staehelin, L.A. (1976). Functional significance of the variations in the geometrical organization of tight junction networks. J. Cell Biol. *68*, 688–704.

Itoh, M., Nagafuchi, A., Moroi, S., and Tsukita, S. (1997). Involvement of ZO-1 in cadherin-based cell adhesion through its direct binding to alpha catenin and actin filaments. J. Cell Biol. *138*, 181–192.

Ivanov, A.I., Parkos, C.A., and Nusrat, A. (2010). Cytoskeletal regulation of epithelial barrier function during inflammation. Am. J. Pathol. *177*, 512–524.

Leerberg, J.M., Gomez, G.A., Verma, S., Moussa, E.J., Wu, S.K., Priya, R., Hoffman, B.D., Grashoff, C., Schwartz, M.A., and Yap, A.S. (2014). Tension-sensitive actin assembly supports contractility at the epithelial zonula adherens. Curr. Biol. *24*, 1689–1699.

Macara, I.G., Guyer, R., Richardson, G., Huo, Y., and Ahmed, S.M. (2014). Epithelial homeostasis. Curr. Biol. *24*, R815–R825.

Machacek, M., Hodgson, L., Welch, C., Elliott, H., Pertz, O., Nalbant, P., Abell, A., Johnson, G.L., Hahn, K.M., and Danuser, G. (2009). Coordination of Rho GTPase activities during cell protrusion. Nature *461*, 99–103.

Nieuwkoop, P.D. (1994). Normal Table of Xenopus laevis (Daudin) (Garland Science).

Oda, Y., Otani, T., Ikenouchi, J., and Furuse, M. (2014). Tricellulin regulates junctional tension of epithelial cells at tricellular contacts through Cdc42. J. Cell. Sci. *127*, 4201–4212.

Pitelka, D.R., and Taggart, B.N. (1983). Mechanical tension induces lateral movement of intramembrane components of the tight junction: studies on mouse mammary cells in culture. J. Cell Biol. *96*, 606–612.

Pitelka, D.R., Taggart, B.N., and Hamamoto, S.T. (1983). Effects of extracellular calcium depletion on membrane topography and occluding junctions of mammary epithelial cells in culture. J. Cell Biol. *96*, 613–624.

Pope, K.L., and Harris, T.J.C. (2008). Control of cell flattening and junctional remodeling during squamous epithelial morphogenesis in Drosophila. Development *135*, 2227–2238.

Priya, R., Gomez, G.A., Budnar, S., Verma, S., Cox, H.L., Hamilton, N.A., and Yap, A.S. (2015). Feedback regulation through myosin II confers robustness on RhoA signalling at E-cadherin junctions. Nat. Cell Biol. *17*, 1282–1293.

Quiros, M., and Nusrat, A. (2014). RhoGTPases, actomyosin signaling and regulation of the epithelial apical junctional complex. Semin. Cell Dev. Biol. *36*, 194–203.

Razzell, W., Wood, W., and Martin, P. (2014). Recapitulation of morphogenetic cell shape changes enables wound re-epithelialisation. Development *141*, 1814–1820.

Reyes, C.C., Jin, M., Breznau, E.B., Espino, R., Delgado-Gonzalo, R., Goryachev, A.B., and Miller, A.L. (2014). Anillin regulates cell-cell junction integrity by organizing junctional accumulation of Rho-GTP and actomyosin. Curr. Biol. *24*, 1263–1270.

Richter, J.F., Schmauder, R., Krug, S.M., Gebert, A., and Schumann, M. (2016). A novel method for imaging sites of paracellular passage of macromolecules in epithelial sheets. J. Control. Release *229*, 70–79.

Rizvi, S.A., Neidt, E.M., Cui, J., Feiger, Z., Skau, C.T., Gardel, M.L., Kozmin, S.A., and Kovar, D.R. (2009). Identification and characterization of a small molecule inhibitor of formin-mediated actin assembly. Chem. Biol. *16*, 1158–1168.

Rosenthal, R., Günzel, D., Theune, D., Czichos, C., Schulzke, J.D., and Fromm, M. (2017). Water channels and barriers formed by claudins. Ann. N. Y. Acad. Sci. *1397*, 100–109.

Rothen-Rutishauser, B., Riesen, F.K., Braun, A., Günthert, M., and Wunderli-Allenspach, H. (2002). Dynamics of tight and adherens junctions under EGTA treatment. J. Membr. Biol. *188*, 151–162.

Sasaki, H., Matsui, C., Furuse, K., Mimori-Kiyosue, Y., Furuse, M., and Tsukita, S. (2003). Dynamic behavior of paired claudin strands within apposing plasma membranes. Proc. Natl. Acad. Sci. U S A *100*, 3971–3976.

Session, A.M., Uno, Y., Kwon, T., Chapman, J.A., Toyoda, A., Takahashi, S., Fukui, A., Hikosaka, A., Suzuki, A., Kondo, M., et al. (2016). Genome evolution in the allotetraploid frog Xenopus laevis. Nature *538*, 336–343.

Shao, Y., Wolf, P.G., Guo, S., Guo, Y., Gaskins, H.R., and Zhang, B. (2017). Zinc enhances intestinal epithelial barrier function through the PI3K/AKT/mTOR signaling pathway in Caco-2 cells. J. Nutr. Biochem. *43*, 18–26.

Shen, L., and Turner, J.R. (2005). Actin depolymerization disrupts tight junctions via caveolae-mediated endocytosis. Mol. Biol. Cell *16*, 3919–3936.

Shen, L., Weber, C.R., and Turner, J.R. (2008). The tight junction protein complex undergoes rapid and continuous molecular remodeling at steady state. J. Cell Biol. *181*, 683–695.

Shen, L., Weber, C.R., Raleigh, D.R., Yu, D., and Turner, J.R. (2011). Tight junction pore and leak pathways: a dynamic duo. Annu. Rev. Physiol. *73*, 283–309.

Thumkeo, D., Watanabe, S., and Narumiya, S. (2013). Physiological roles of Rho and Rho effectors in mammals. Eur. J. Cell Biol. *92*, 303–315.

Tokuda, S., Hirai, T., and Furuse, M. (2016). Effects of osmolality on paracellular transport in MDCK II cells. PLoS One *11*, e0166904.

Trichas, G., Smith, A.M., White, N., Wilkins, V., Watanabe, T., Moore, A., Joyce, B., Sugnaseelan, J., Rodriguez, T.A., Kay, D., et al. (2012). Multi-cellular rosettes in the mouse visceral endoderm facilitate the ordered migration of anterior visceral endoderm cells. PLoS Biol. *10*, e1001256.

Turner, J.R., Buschmann, M.M., Romero-Calvo, I., Sailer, A., and Shen, L. (2014). The role of molecular remodeling in differential regulation of tight junction permeability. Semin. Cell Dev. Biol. *36*, 204–212.

Van Itallie, C.M., and Anderson, J.M. (2014). Architecture of tight junctions and principles of molecular composition. Semin. Cell Dev. Biol. *36*, 157–165.

Van Itallie, C.M., Fanning, A.S., Bridges, A., and Anderson, J.M. (2009). ZO-1 stabilizes the tight junction solute barrier through coupling to the perijunctional cytoskeleton. Mol. Biol. Cell *20*, 3930–3940.

Van Itallie, C.M., Tietgens, A.J., and Anderson, J.M. (2017). Visualizing the dynamic coupling of claudin strands to the actin cytoskeleton through ZO-1. Mol. Biol. Cell *28*, 524–534.

Van Itallie, C.M., Tietgens, A.J., Krystofiak, E., Kachar, B., and Anderson, J.M. (2015). A complex of ZO-1 and the BAR-domain protein TOCA-1 regulates actin assembly at the tight junction. Mol. Biol. Cell *26*, 2769–2787.

Wallingford, J.B., Ewald, A.J., Harland, R.M., and Fraser, S.E. (2001). Calcium signaling during convergent extension in Xenopus. Curr. Biol. *11*, 652–661.

Wang, X., Valenzano, M.C., Mercado, J.M., Zurbach, E.P., and Mullin, J.M. (2013). Zinc supplementation modifies tight junctions and alters barrier function of CACO-2 human intestinal epithelial layers. Dig. Dis. Sci. *58*, 77–87.

Webb, S.E., and Miller, A.L. (2006). Ca2+ signaling and early embryonic patterning during the blastula and gastrula periods of zebrafish and Xenopus development. Biochim. Biophys. Acta *1763*, 1192–1208.

Xiao, R., Yuan, L., He, W., and Yang, X. (2018). Zinc ions regulate opening of tight junction favouring efflux of macromolecules via the GSK3β/snail-mediated pathway. Metallomics *10*, 169–179.

Yu, D., Marchiando, A.M., Weber, C.R., Raleigh, D.R., Wang, Y., Shen, L., and Turner, J.R. (2010). MLCK-dependent exchange and actin binding region-dependent anchoring of ZO-1 regulate tight junction barrier function. Proc. Natl. Acad. Sci. U S A *107*, 8237–8241.

Zihni, C., Mills, C., Matter, K., and Balda, M.S. (2016). Tight junctions: from simple barriers to multifunctional molecular gates. Nat. Rev. Mol. Cell Biol. *17*, 564–580.

STAR★METHODS

KEY RESOURCES TABLE

REAGENT or RESOURCE	SOURCE	IDENTIFIER
Chemicals, Peptides, and Recombinant Proteins		
FluoZin-3	Thermo Fisher Scientific	Cat #: F24194
Latrunculin B	Sigma	Cat#: L5288-1MG; CAS #: 76343-94-7
(S)-H-1152 (hydrochloride)	Cayman Chemicals	Cat #: 10007653; CAS #: 451462-58-1
SMIFH2	Tocris	Cat #: 4401; CAS #: 340316-62-3
Y-27632	Calbiochem/Millipore	Cat #: 688000-1MG; CAS #: 146986-50-7
Experimental Models: Organisms/Strains		
Oocyte Positive Female *Xenopus laevis*, Pigmented	Nasco	Cat #: LM00531
Oocyte Positive Female *Xenopus laevis*, Albino	Nasco	Cat #: LM00531(A)
Male (Mature) 7.5-9 cm *Xenopus laevis*, Pigmented	Nasco	Cat #: LM00715
Xla.NXT-WT:Albino^{NXR} (females)	National *Xenopus* Resource	NXR_0.0082
Xla.NXR-WT^{NXR} (males)	National *Xenopus* Resource	NXR_0.0031
Oligonucleotides		
Primers for creating pCS2+/BFP-ZO-1: F: TTTACCCGGGATGTCCGCCAGAGCT R: CTGGGAGCTCTTAAAAGTGGTCAATAAGGAC		N/A
Primers for creating pCS2+/mRFP-ZO-1 ΔABR: primers above for BFP-ZO-1 plus: N-frag R: GATGCTCTAGGTGCCTGTTCG C-frag F: GAACAGGCACCTAGAGCATCACACAT TGCTGCCAGCCATCTCTCC		N/A
Primers for creating pCS2+/mCherry-occludin: F: ACTGAGATCTATGTCCGCCAGGCCATTTG R: CAGTGAATTCTTATTTGCCATTGTCATAGT CGCTGAC		N/A
Recombinant DNA		
pCS2+/GFP-rGBD	Benink and Bement, 2005	N/A
pCS2+/mRFP-ZO-1	Higashi et al., 2016	N/A
pCS2+/mCherry-claudin-6	Higashi et al., 2016	N/A
pCS2+/mCherry-farnesyl	Reyes et al., 2014	N/A
pCS2+/Lifeact-RFP	Higashi et al., 2016	N/A
pCS2+/Lifeact-GFP	Higashi et al., 2016	N/A
pCS2+/BFP-membrane	Higashi et al., 2016	N/A
pCS2+/E-cadherin-3xmCherry	Higashi et al., 2016	N/A
pCS2+/mCherry-α-catenin	Higashi et al., 2016	N/A
pCS2+/mCherry-angulin-1-3xGFP	Higashi et al., 2016	N/A
pCS2+/mCherry-tricellulin	Higashi et al., 2016	N/A
pCS2+/3xGFP-Dia3	Higashi et al., 2019	N/A
pCS2+/mCherry-2xrGBD	Gift from W.M. Bement (University of Wisconsin, Madison); Davenport et al., 2016	N/A
pCS2+/BFP-2xrGBD	Gift from W.M. Bement (University of Wisconsin, Madison); Davenport et al., 2016	N/A
pCS2+/BFP-ZO-1	this study	N/A
pCS2+/mRFP-ZO-1 ΔABR	this study	N/A
pCS2+/mCherry-occludin	this study	N/A

(*Continued on next page*)

Continued

REAGENT or RESOURCE	SOURCE	IDENTIFIER
pCS2+/SF9-mNeon	Arnold et al., 2019	N/A
cDNA: *X. laevis* occludin	Thermo Fisher	(Clone ID: 7009477)
Software and Algorithms		
Microsoft Excel for Mac version 15.15		N/A
Graphpad Prism 7		N/A
Fiji		N/A
Volocity version 6.3	Perkin Elmer	N/A
SciPy.stats package (function mannwhitneyu)		N/A
Custom code for generating kymographs (see STAR Methods)	This study	N/A
NumPy (python package)		N/A
OpenCV2 (python package)		N/A
Pandas (python package)		N/A
Shapely (python package)		N/A
ImageIO (python package)		N/A
Other		
National *Xenopus* Resource		RRID:SCR_013731
Xenbase http://www.xenbase.org/		RRID:SCR_003280

CONTACT FOR REAGENT AND RESOURCE SHARING

Further information and requests for resources and reagents should be directed to and will be fulfilled by the Lead Contact, Ann L. Miller (annlm@umich.edu).

EXPERIMENTAL MODEL AND SUBJECT DETAILS

Adult *Xenopus laevis* wild type or albino female frogs and wild type male frogs were purchased from Nasco (Ft. Atkinson, WI) or the National *Xenopus* Resource (Woods Hole, MA). Female frogs were injected with human chorionic gonadotropin (HCG) to induce them to lay eggs. Male frogs were used for acquisition of testes for sperm preparations. *Xenopus laevis* eggs were collected, fertilized *in vitro*, dejellied in 2% cysteine, pH 7.8 (Sigma), and embryos were cultured in 0.1xMMR (10 mM NaCl, 200 μM KCl, 200 μM $CaCl_2$, 100 μM $MgCl_2$, 500 μM HEPES, pH 7.4). At the 2- or 4-cell stage, embryos were microinjected with mRNA and were allowed to develop to gastrula stage (Nieuwkoop and Faber stage 10-12; Nieuwkoop, 1994).

Frogs were housed in a recirculating tank system (Tecniplast, Milan, Italy), which constantly monitors the following water quality parameters: temperature, pH, and conductivity to ensure safe and consistent water quality for an optimal environment for frog health. Daily health and maintenance checks were performed by Animal Care Staff, and frogs were fed frog brittle (Nasco, Ft. Atkinson, WI) two times per week.

All studies strictly adhered to the compliance standards of the US Department of Health and Human Services Guide for the Care and Use of Laboratory Animals and were approved by the University of Michigan's Institutional Animal Care and Use Committee. A board-certified Laboratory Animal Veterinarian oversees our animal facility.

METHOD DETAILS

Generation of New DNA Constructs

Primers for the described constructs are listed in the key resources table. pCS2+/BFP-ZO-1 was generated by PCR amplification of human ZO-1 from pCS2+/mRFP-ZO-1 (Higashi et al., 2016) and cloned into pCS2+/N-BFP. pCS2+/mRFP-ZO-1 ΔABR was made by deleting base pairs 3456-4116 (corresponding to amino acids 1152-1371) from human ZO-1. The N- and C-terminal fragments of ZO-1 needed to make this deletion mutant were amplified with PCR, stitched together using splicing by overlap extension (SOEing) PCR, and cloned into pCS2+/N-mRFP. pCS2+/mCherry-occludin was generated by amplifying *X. laevis* occludin from a cDNA clone purchased from Thermo Fisher (Clone ID: 7009477) and cloned into pCS2+/N-mCherry. All DNA constructs were verified by sequencing (GENEWIZ, South Plainfield, NJ).

mRNA Preparation and Microinjection

mRNAs were transcribed *in vitro* from pCS2+ vectors using the mMessage mMachine SP6 kit (Ambion) and purified using the RNeasy kit (Qiagen). Prior to *in vitro* transcription, plasmid DNA was linearized with NotI (except for constructs containing ZO-1, which were linearized using KpnI). mRNAs were mixed together and microinjected into 2- to 4-cell stage embryos at 4 distinct locations in the animal hemisphere. Each 5 nl injection contained the following amount of the appropriate mRNAs: GFP-rGBD: 80 pg, mCherry-2xrGBD: 40 pg, BFP-2xrGBD: 33 pg, BFP-ZO-1: 70 pg, mRFP-ZO-1: 220 pg, mRFP-ZO-1 ΔABR: 210 pg, mCherry-claudin-6: 14 pg, mCherry-occludin: 6 pg, mCherry-farnesyl: 50 pg, Lifeact-RFP: 12.5 pg, Lifeact-GFP: 12.5 pg, SF9-mNeon: 20-40 pg, BFP-membrane: 12.5 pg, E-cadherin-3xmCherry: 40 pg, mCherry-α-catenin: 40 pg, angulin-1-3xGFP: 25 pg, mCherry-tricellulin: 1.75 pg, 3xGFP-Dia3: 25 pg.

Live Imaging

Live confocal laser scanning microscopy of gastrula-stage *Xenopus laevis* embryos was performed at room temperature with an inverted Olympus Fluoview 1000 equipped with FV10-ASW software using either a 60X Plan Apo N supercorrected objective (NA = 1.4, working distance = 0.12 mm) or a 20X Plan S-Apo objective (NA = 0.85, working distance = 0.17 mm). Embryos were mounted in a custom chamber consisting of a 0.8 mm-thick metal slide with a 5-10 mm hole in the center and a coverslip attached to one side with a thin layer of vacuum grease. Embryos were placed in this chamber with 0.1xMMR (or other specified media) and gently compressed with a second coverslip also adhered with vacuum grease. The slide was inverted to image the animal hemisphere of the embryo. When solutions were added to the embryos during live imaging (e.g. EGTA), the first coverslip was placed so that it only partially covered the hole, leaving an opening through which liquid can be applied by pipetting during imaging once the slide is inverted.

Generally, imaging of Rho flares was performed by collecting the 3 most apical *z*-planes with a 60X objective and 2X digital zoom, a scan speed of 2 μs/pixel, and a step size of 0.5 μm for tight junction proteins (ZO-1, occludin, claudin-6, angulin-1, tricellulin), membrane (farnesyl), F-actin (Lifeact) (time interval: 5 seconds), or 0.75 μm for E-cadherin and α-catenin (time interval: 6 seconds). For myosin II (SF9), the 4 most apical z-planes were imaged with a 4 μs/pixel scan speed and a step size of 0.5 μm (time interval: 10 seconds). Generally, for imaging ZnUMBA, the 6-8 most apical *z*-planes were collected with a 60X objective and a 1.5X digital zoom, a step size of 0.5 μm and a scan speed of 8 μs/pixel (time interval: 15-21 seconds). The ZnUMBA/EGTA experiments were imaged with a 20X objective, a scan speed of 8 μs/pixel, and a step size of 1.55 μm for 5 z-planes (time interval: 28 seconds). In each case, channels were acquired sequentially by line to minimize bleedthrough.

Zinc-Based Ultrasensitive Microscopic Barrier Assay

To carry out the Zinc-based Ultrasensitive Microscopic Barrier Assay (ZnUMBA), 5-10 nl of 1 mM FluoZin3 (Thermo Fisher Scientific), 100 μM $CaCl_2$, and 100 μM EDTA was microinjected into the blastocoel of stage 10-11 (Nieuwkoop and Faber) *X. laevis* embryos. EDTA was used to reduce baseline levels of FluoZin3 fluorescence from endogenous Zn^{++}, and equimolar Ca^{++} was added to offset the potential effects of Ca^{++} chelation by EDTA. Albino embryos were used to better visualize the blastocoel during microinjection. Embryos were allowed to heal from the microinjection wound for a minimum of 5 minutes before being mounted in a slide containing 1-2 mM $ZnCl_2$ in 0.1xMMR. Embryos were imaged with confocal microscopy immediately after mounting. Relative increases in FluoZin3 fluorescence were interpreted as breaches in the barrier.

Drug Treatments

Latrunculin B (Sigma) was resuspended in DMSO to a concentration of 1 mM and stored in aliquots at -20° C. Just prior to imaging, embryos were mounted in 0.1xMMR containing Latrunculin B. A range of 8-10 μM was used to achieve a severe effect, and 1-5 μM was used to produce a mild effect.

Y-27632 (Calbiochem) was resuspended in DMSO to a concentration of 30 mg/ml and stored in aliquots at -20° C. Y-27632 or an equivalent amount of DMSO was mixed with probe mRNA and microinjected into embryos at the 2- or 4-cell stage. A total of 1.5 ng Y-27632 was injected into each embryo.

SMIFH2 (Tocris) was resuspended in DMSO to a concentration of 10 mM, aliquoted, snap frozen in liquid nitrogen, and stored at -80° C. Immediately before imaging, an aliquot of SMIFH2 was thawed and diluted to 100 μM in 0.1xMMR. Embryos were placed in this solution (or the equivalent amount of DMSO in 0.1xMMR), mounted on a slide, and imaged for up to 1 hour.

For the experiments in Figures S5E–S5H, H-1152 (Cayman Chemicals) was resuspended in DMSO to a concentration of 10 mM and stored in aliquots at -20° C. 5 nl of H-1152 or DMSO was directly injected into the blastocoel of gastrula-stage albino embryos, which were then incubated at room temperature for 30 to 90 minutes prior to imaging.

For the ZnUMBA experiments in Figure 6, H-1152 (Cayman Chemicals) was resuspended to 10 mM in water on the day of the experiment and stored on ice. 10 nl of H-1152 or water was injected into the blastocoel of albino embryos that had previously been injected with FluoZin3. Embryos were incubated at room temperature for 10 minutes before being mounted in media containing Zn^{++} with or without SMIFH2.

Junction Injury

Junction injury was performed on albino embryos using a 405 nm laser and SIM scanner on the microscope described above. A small circular ROI was placed at the junction, and the 405 nm laser was pulsed in the ROI for 15 seconds at 70% power. These settings

were sufficient to induce an injury response roughly half the time and photobleaching in the other cases. Substantial recoil was not observed with these settings.

QUANTIFICATION AND STATISTICAL ANALYSIS

Figure Preparation

Images were processed in Fiji. First, z-planes were summed, and the channels were independently adjusted to highlight relevant features in the image using linear adjustments that cover the full range of data. LUTs were applied as described in the figure legends. With the exception of the kymographs in Figures 5A, S4A, and S4B, images were enlarged in Photoshop CS6 using bicubic interpolation.

Manual Quantification of Flares

Flare Selection

We defined flares as transient increases in active Rho that arise from cell-cell junctions. Thus, we only included accumulations of active Rho that increased, peaked, and decreased within 1-4 minutes. Static or sustained increases in active Rho were not considered in the analysis. To simplify the analysis, we only included flares that were isolated in space and time from other flares over the time span to be analyzed (i.e., no other flares at the same location for 500 seconds before or after the flare). An exception is when drug treatments resulted in a limited number of non-repeating flares (e.g., Figure 5G).

Flare Measurements

Flare measurements were performed in Fiji on summed z-projections of unprocessed images. The intensity of a small circular region of interest (ROI) with a diameter of 0.75 μm (exceptions for ZnUMBA: 1.3 μm diameter; tricellulin and angulin-1: 1.7 μm diameter) was used to measure fluorescence intensity of active Rho and accompanying probes. The ROI was placed on the junction at the approximate site of the flare and was moved manually each frame to account for cell and embryo movement. A custom macro was used to measure each channel and advance the frame. To account for photobleaching and focal drift, each measurement was normalized to a reference ROI (measured as described above) on a nearby junction. Each flare was measured in triplicate with three distinct reference ROIs. The baseline was normalized to 1 by dividing the value for each frame by the average intensity of the first ten frames. Flares were aligned on the x-axis so that the frame immediately before the rapid increase in Rho activity corresponds to time 0. Rapid increase in intensity was defined by consecutive increases in Rho intensity of at least 5% of baseline for at least three of four frames. Graphs are the mean of the normalized intensity of multiple flares. The number of flares, embryos, and experiments is indicated in the figure legend. Error bars represent standard error of the mean unless otherwise stated in the figure legend.

Kymograph Construction and Analysis

Image and data analysis were performed with the help of Fiji and custom Python scripts using NumPy, SciPy, OpenCV, Matplotlib, pandas and other open source libraries.

Kymograph Construction

Cell-cell junction positions were digitized from ZO-1 or occludin images with the use of watershed and active vector graph algorithms (Genovesio, 2009). The intensity of circular ROI (diameter 0.75 μm) centered at points on cell-cell junctions was used to measure fluorescence of active Rho and accompanying channels along the cell-cell junctions forming one horizontal line of the kymograph. The stacking of center-aligned lines of successive frames resulted in the kymograph of the cell-cell junction.

Flare Analysis

Flare candidates were detected using thresholding of the normalized Rho channel. Candidates were then filtered out using the following criteria: 1) minimal size of 5 pixels; 2) flare located mostly on one cell-cell junction; 3) there are at least 8.3 minutes of recording before and after the flare; 4) no other flares on the same junction within 5 minutes; 5) flare is not located on a junction associated with the cleavage furrow of a dividing cell within 8 minutes. The selected flare was identified on a corresponding junction kymograph, and a vertical path corresponding to the location of the flare on a junction was specified with the help of kymograph fiducial marks. The path points were translated back to the original frames and signal intensity of active Rho and accompanying channels was collected at these points as the averaged intensity of the circular ROI (diameter 0.75 μm). Reference values were calculated as the median of the intensity distribution on the junctions.

Normalized intensity was calculated as $I_{norm} = \frac{I_{signal}}{I_{reference}}$ and normalized to a baseline of ~1 by dividing the value for each frame by the median intensity of the first 6.5 minutes. Flares were aligned on the x-axis (time) so that the moment before the rapid increase in Rho activity corresponds to time 0 (that was achieved by fitting ramp function $I=c+k\,R(t-t_0)$ on the interval near the maximum slope of active RhoA signal). Graphs are the mean of the normalized intensity of the number of flares indicated in the figure legend; error bars represent standard error of the mean unless otherwise stated in the figure legend.

Calculation of Flare Frequency

We counted the flares from seven videos of embryos expressing GFP-rGBD and mCherry-occludin to mark the junctions. A flare was classified as bicellular if it was located on a single cell-cell junction and multicellular if it overlapped two or more cell-cell junctions. As described above, we only included flares that were isolated in space and time from other flares over the time span to be analyzed. We

obtained the average frequency f_i of bicellular and multicellular junctions and averaged those numbers with weights w_i corresponding to the length of the videos. Because all videos were recorded at the same dimensions and magnification, there was no need to account for the area of the recordings in weights. Thus, we obtained the weighted mean frequency $\bar{f}$. We also estimated standard error of weighted mean:

$$\bar{f} = \frac{\sum w_i f_i}{\sum w_i}, \quad SEM = \sqrt{\frac{1}{N-1}\frac{\sum w_i \left(f_i - \bar{f}\right)^2}{\sum w_i}}.$$

Statistics

Standard error of the mean was calculated in Microsoft Excel version 15 or GraphPad Prism 7. To determine significance, one-sided Mann–Whitney U tests were performed with the help of open source SciPy.stats package (function mannwhitneyu).

DATA AND SOFTWARE AVAILABILITY

The data that support the findings of this study are available from the Lead Contact upon reasonable request. Custom code used in this study is available at: https://github.com/GoryachevAB-group/junction-signal-processing.